GEM TN-92-91

Progress Report: Neutron Flux in the GEM Detector

David M. Lee, R.E. Prael, Laurie Waters
Los Alamos National Laboratory

April 4, 1992

Abstract:

The status of neutron fluence calculations throughout the GEM detector using the LAHET/MCNP code is described. Included are studies of fluence through the silicon vertex detector, and suppression obtainable with borated polyethylene. Also addressed are fluences within the endcap and forward calorimeters, as well as along the first muon chamber after the endcap. This report will be updated as new results are obtained, and old calculations are redone to reflect changes in detector geometry and materials.

6.2 NEUTRON FLUENCE IN THE GEM DETECTOR

A group of simulation codes available at Los Alamos are now being used to evaluate the radiation environment of the GEM detector. The Los Alamos High Energy Transport (LAHET) code[1] is a monte carlo code which interfaces with the low energy neutron (less than 20 MeV) monte carlo package MCNP[2]. LAHET has recently been extended to include the FLUKA[3] monte carlo code to handle high energy hadronic cascades, while retaining the Los Alamos version of HETC[4] for lower energies[5][1]. Electromagnetic processes are analyzed with EGS4[6]. The residual nuclei produced by LAHET, and the neutron flux less than 20 MeV from MCNP are then input into the CINDER90[7] code to provide activation calculations for detector components. The CINDER90 code also produces photon spectra from the activation products which are used as a sources in MCNP for transport to areas around the detector where personal safety is of concern, and radiation dose-equivalents calculated.

This report gives the status of the current and ongoing LANL calculations. It will be frequently updated as new results are obtained, and as old calculations are redone to reflect changes in materials and geometry. Please note only neutron fluence calculations are described in this writing. Similar results may be obtained for any other particle, charged or neutral, and will be reported in the near future.

The radiation environment at the SSC has been addressed in several previous works. Most notable is the work of the Task Force headed by D. E. Groom[8]. In addition, the study of the L* detector carried out at Los Alamos in 1991[9] has provided important guidelines for the GEM work presented below. This study is designed to present, on a timely basis, the most detailed calculations yet possible of GEM, for neutron and other particle backgrounds in the detector, the effects of such backgrounds on detector signals, activation of elements, and radiation dose calculations.

6.2.1 Input, Output and Running Conditions

Unless indicated otherwise, results presented in this report are based on input from 50 ISAJET events[10], run in the TWOJET mode with cuts on Pt from 4 to 100 GeV/c. These cuts are chosen to simulate minimum bias events[2]. Exactly the same events are used for each study, and presently, only incident charged pions, protons and neutrons are used. Figure 1 illustrates the $dn/d\eta$ spectra for these particles, plots which are helpful in evaluating how the input fluctuates in various acceptances.

The particle background results are presented in terms of Flux, Fluence or Current. Current represents a simple counting of particles crossing a particular surface. Results are occasionally broken down according to the angle the particle direction makes with the

[1]Currently HETC is used for hadrons with kinetic energies less than 2GeV, and FLUKA exclusively above 5GeV. The two codes are phased in linearly between 2 and 5GeV. These limits are adjustable by the user.

[2]private communication, Frank Paige

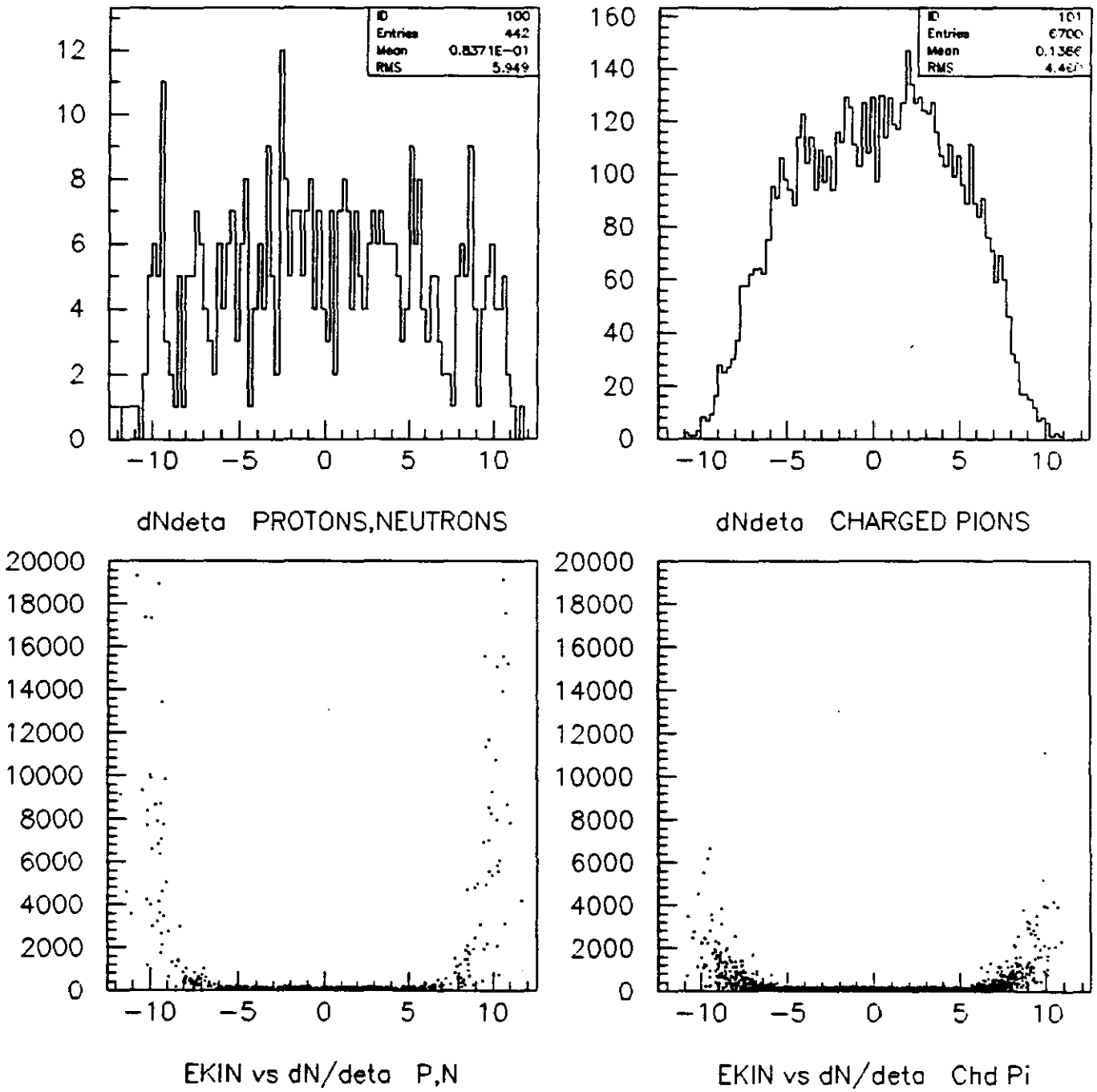

Figure 1: Pseudorapidity distributions, and energy versus η for all protons, neutrons and charged pions from the 50 ISAJET events used in these simulations. The figure on the next page shows the energy versus η distribution of the original jets from which the final state particles were produced.

waters/4-4-92

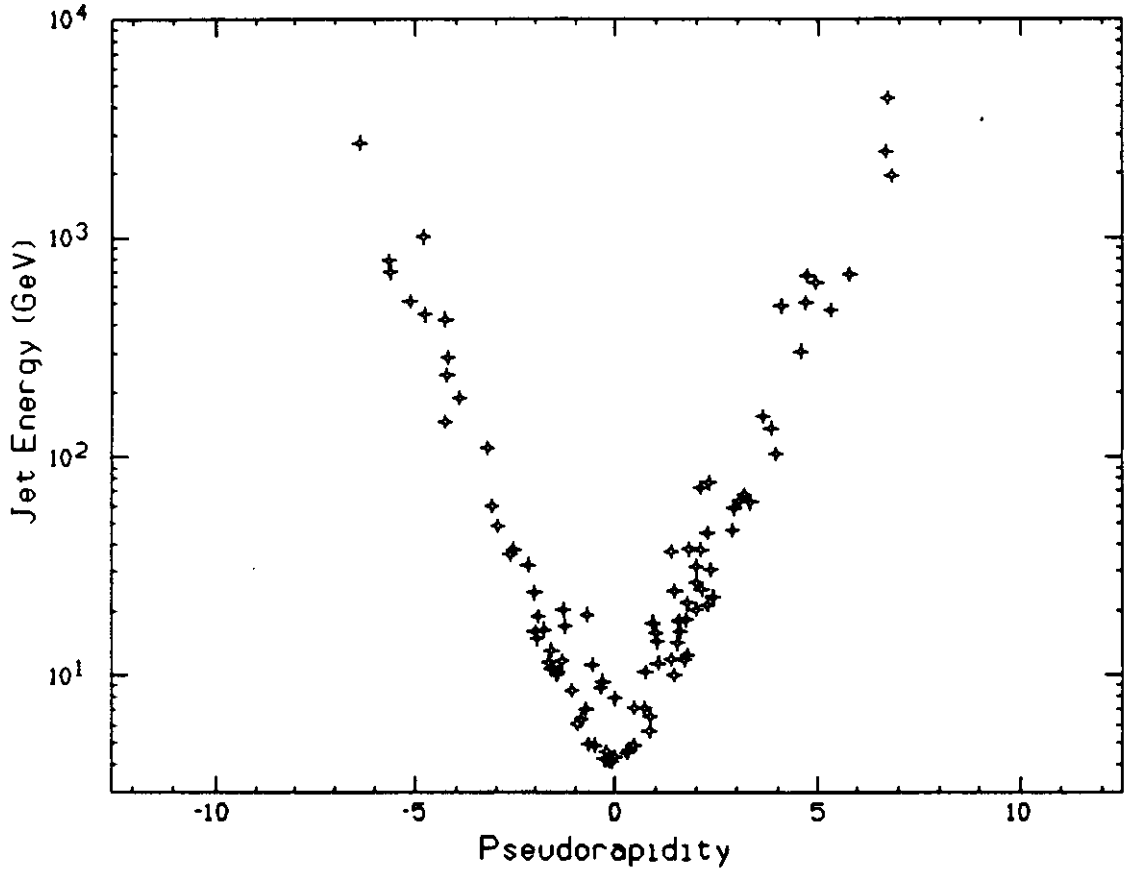
Jet Energy (GeV)
Pseudorapidity
10^4
10^3
10^2
10^1
-10
-5
0
5
10

surface normal vector. The LAHET/MCNP packages assign a weighting factor to each produced particle, and it is this value which is incremented in all sums. The reader is referred to the MCNP manual[2] for information on the various sources of such weights. In the Flux and Fluence data, each particle is further weighted by the inverse of the absolute value of the cosine the particle direction makes with the surface normal. 'Fluence' refers to a time integrated sum, either over 1 SSC minimum bias event, or over 1 SSC year (1×10^7 seconds). The units of 'Flux' are number of particles per second. (We use 1×10^8 minimum bias events per second, which assumes 1.6 minbias events per beam crossing, and one beam crossing every 16 nsec.) Electrons and photons may also be tracked with the EGS4 code, but the present studies do not depend on electromagnetic processes.

No magnetic field has currently been implemented. This is not considered crucial for the present neutron studies since the detector is azimuthally symmetric, which is the same direction charged particles will bend. A gaussian approximation to energy straggling is used, and multiple scattering is applied to all tracked charged particles. Particles are tracked down to the thresholds summarized in Table 1.

Particle	Threshold
prot, deut, trit, ^{3}He,α, pbar	0.1 MeV
neutrons in Lahet	20.0 MeV
neutrons in MCNP	0.0 MeV
charged pions	149.0 keV
muons	113.0 keV
K+,K-	527.0 keV

Table 1: LAHET/MCNP particle tracking thresholds

6.2.2 GEM Geometry and Materials

Every effort is made to keep up with the most current geometry and materials specifications in the detector. The present results are based on drawings of the barrel and end-cap calorimeters from the 2/19/92 Engineering and Integration Meeting (drawing dated 2/23/92), and the drawing of F. Nimblett (GEM920217) for the muon tracking and field shaper . Figure 2 shows a complete overview of the LAHET geometry. Closeups of this will be displayed as appropriate later in this report.

Supports are modeled with Al5083, which is 96% Al, 4% Mg. The outer beampipe radius is 2.0 cm, containing 1.65 cm vacuum and a .35 cm shell (beryllium out to Z=±1.5m, steel outside this region). Natural iron is used in the field shaper and shield connection since cross section windows in ^{56}Fe are compensated by ^{54}Fe. The excluder regions are presently filled with borated polyethylene. Studies of the detector for several variations in the setup are presented in this report. The effect of substituting the hadronic calorimeter ^{238}U component with Copper is examined. Also, the Copper case is varied by, removing the FCAL material, but leaving the surrounding support structure intact (referred to as the 'No FCAL' case), and by removing virtually all elements in the forward direction with $|Z|>4.776$ meters and $\eta <\sim 3$, including the FCAL and its support structure, the shield in front of the field shaper, and the field shaper itself (referred to as the 'No Forward' case).

Material specifications in the major components for various elements are summarized in Table 2 (note the LAR contains liquid argon and G10/copper readout material, and is contained in the spaces surrounding the calorimetric elements):

	EM	Hadronic	FCAL	LAR
density (gm/cm^3)	4.369	11.861(opt1)	17.022	1.532
		6.2165(opt2)		
elements (#/b/cm)				
^{1}H	.00155	.00595	.0000904	.01519
^{12}C	.00139	.00355	.000199	.01309
^{14}N		.00029	.0000181	.00074
^{16}O	.00082	.00328	.0000362	.00837
^{28}Si	.00020	.00139		.00356
^{40}Ar	.00135	.00453	.00135	.01266
^{52}Cr	.00112	.00140		
Fe_{nat}	.00366	.00461		
^{59}Ni	.00062	.00079	.00607	
^{64}Cu		.047848(opt2)	.00257	.003395
^{184}W			.0526	
^{208}Pb	.00844			
^{238}U		.02703(opt1)		

Table 2: Material specifications for various detector components. Note the separate copper and uranium options for the Hadronic sections. waters/4-4-92

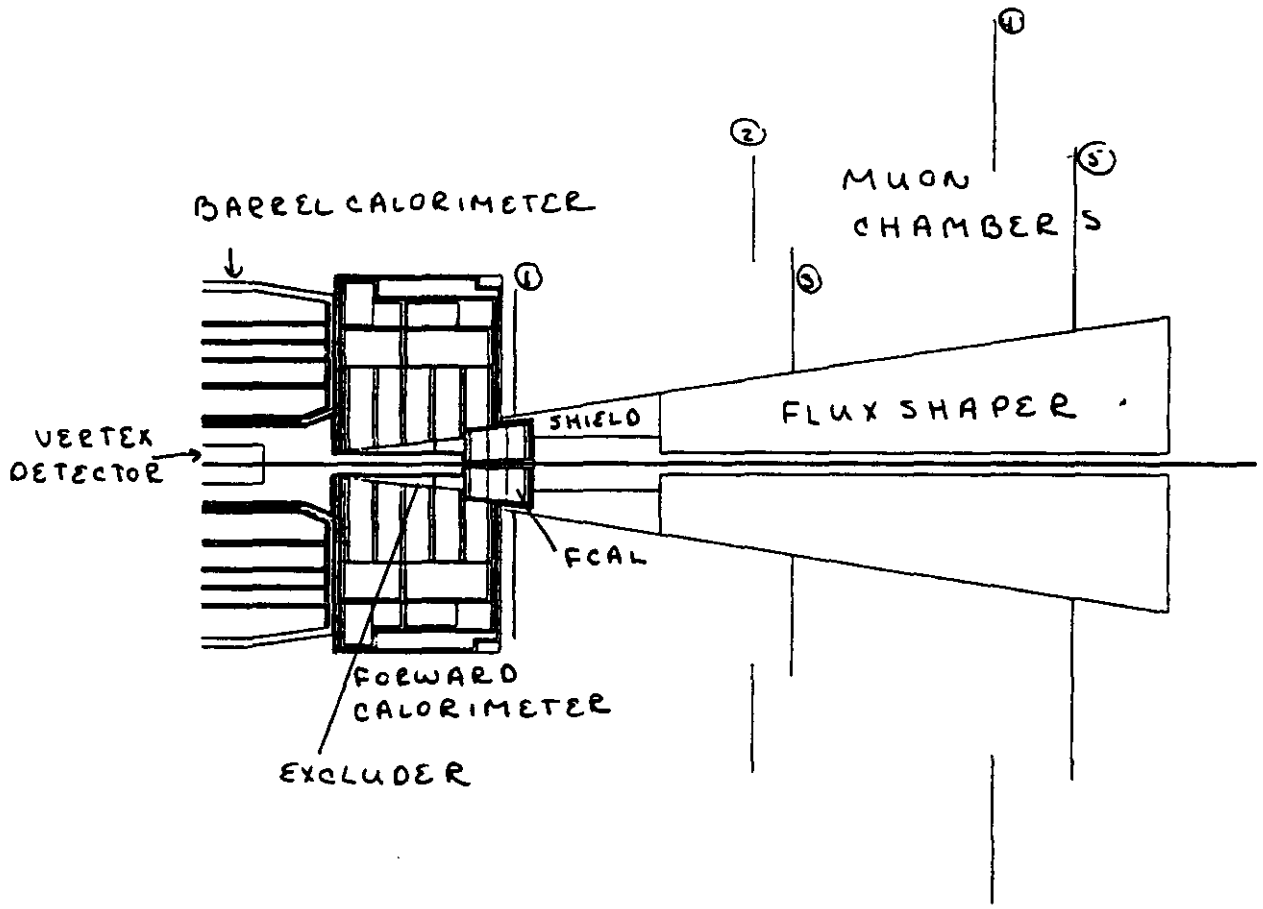

Figure 2: Geometry simulation for LAHET/MCNP for elements Z>0.0. The Detector is symmetric around Z=0.0. waters/4-4-92

6.2.3 Applications

The present status of various code applications are presented below. This report will be continually updated as more results are obtained, and as previously produced results are redone to reflect changes in the GEM setup and material specifications.

6.2.3.1 The Silicon Vertex Detector

The neutron albedo through the cylindrical surface 35 cm in radius and ±100 cm in Z has been evaluated for the GEM configuration described in section 6.2.2. This study was undertaken to ascertain what thickness of borated polyethylene lining in the vertex tracking region is needed to reduce this fluence. Two quantities are most useful in establishing the potential damage to silicon; the fluence of neutrons greater than 100 keV, and the fluence less than 100 keV. As shown in figure 3, the displacement threshold in silicon for neutrons increases by over an order of magnitude above 100 keV, and continues to increase. Neutrons in this energy region are therefore potentially the most damaging. However, one must also keep in mind that the cross section for displacement is non zero below 100 keV, and if the ratio of lower to higher energy neutrons is large, even these low energy particles may be of consequence.

The composition of the shielding material used in these simulations is taken from data given by Reactor Experiments, Inc., catalogue #201, 5% boron-polyethylene. By weight it consists of 61.2% C, 11.6% H, 22.2% ^{16}O, 4% ^{11}B and 1% ^{10}B. The main shielding effect comes from the ^{10}B(n,α)^{7}Li reaction which has a kilobarn cross section for thermal neutrons. The reaction is also accompanied by a .48 MeV gamma. Initial thermalization of the neutrons is achieved through scattering on hydrogen and carbon in the polyethylene.

50 ISAJET events were run in LAHET followed by MCNP, with particle thresholds as described in section 6.2.1. Three cases were considered, no B-poly lining, an overall 5 cm lining, and finally, 5 cm lining the cylindrical surface with 20 cm in the forward directions. The cylindrical portion of the lining extends from a radius of 75 cm to 80 cm, while the forward thicknesses end at z=±235 cm. This area is illustrated in figure 4. Table 3 summarizes the fluence for each case. Please note, these studies were done with the GEM configuration of LLMASON 11/8/91-BWEASOM 1/9/92. This is a slightly larger setup than the one described in section 6.2.2, and tungsten instead of uranium is used in the hadronic calorimeters. We expect similar suppression factors to apply to any general case.

Figure 5 shows the differential fluence (dN/dE) for the three cases as a function of neutron energy. Note the small difference between the 5cm and 5/20cm cases, indicating little is to be gained from larger thicknesses of B-poly. Figure 6 is an analysis of the 5 cm case, in which the composition of the shielding was varied to study the effect of the thermalization provided by the polyethylene, and the absorption of the boron. If the shielding is composed solely of polyethylene, the higher neutron energies are shifted to thermal energies. With the shield composed solely of boron, the extent of the reduction of the thermal component may be seen.

Data for the four variations of the setup described in section 6.2.2 is presented in Table 4. No boron-poly lining is present in these studies. Note the similarity of numbers in all

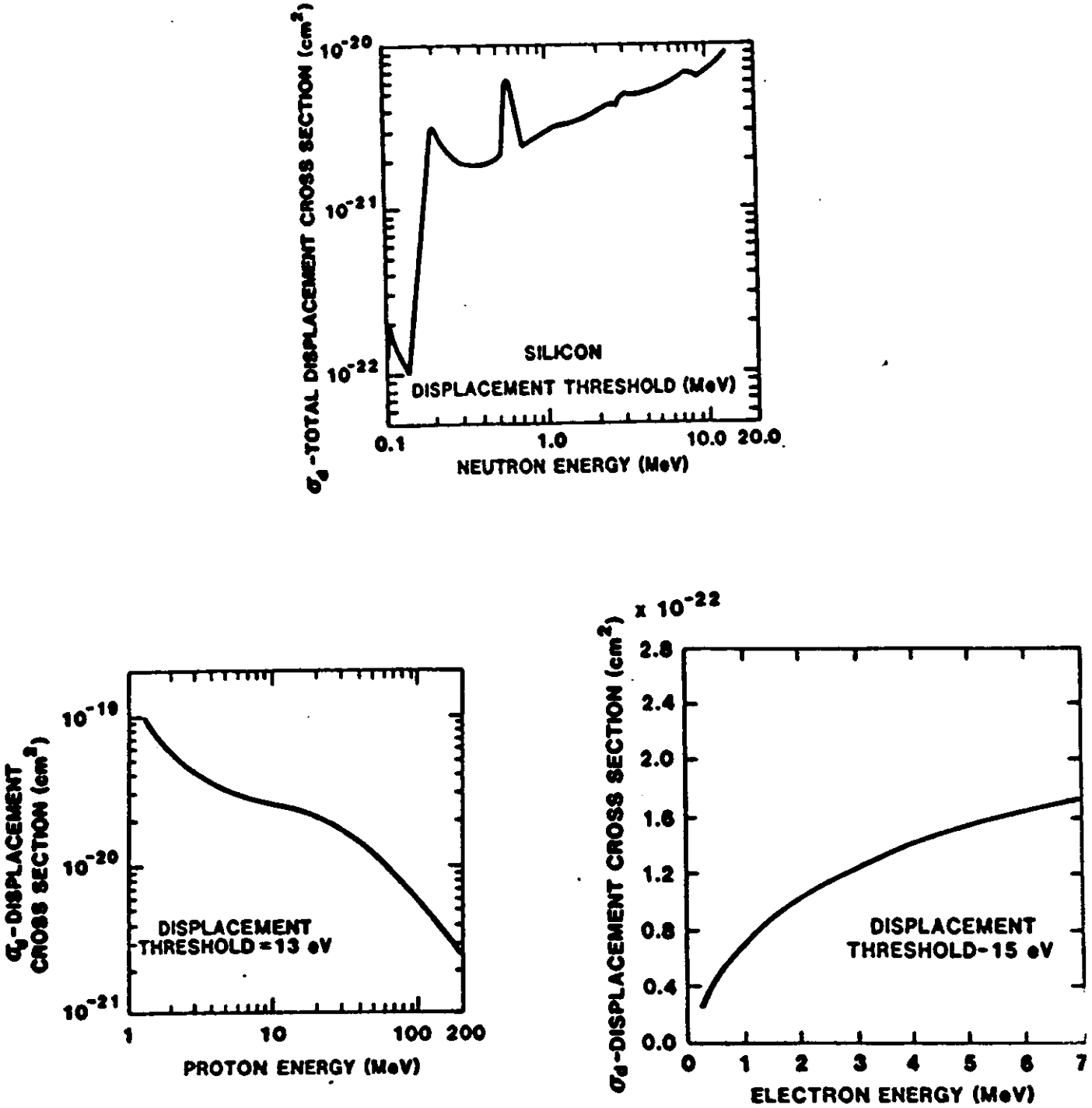

Figure 3: Neutron displacement cross section in Silicon. Proton and Electron displacement cross sections are show for comparison. waters/4-4-92

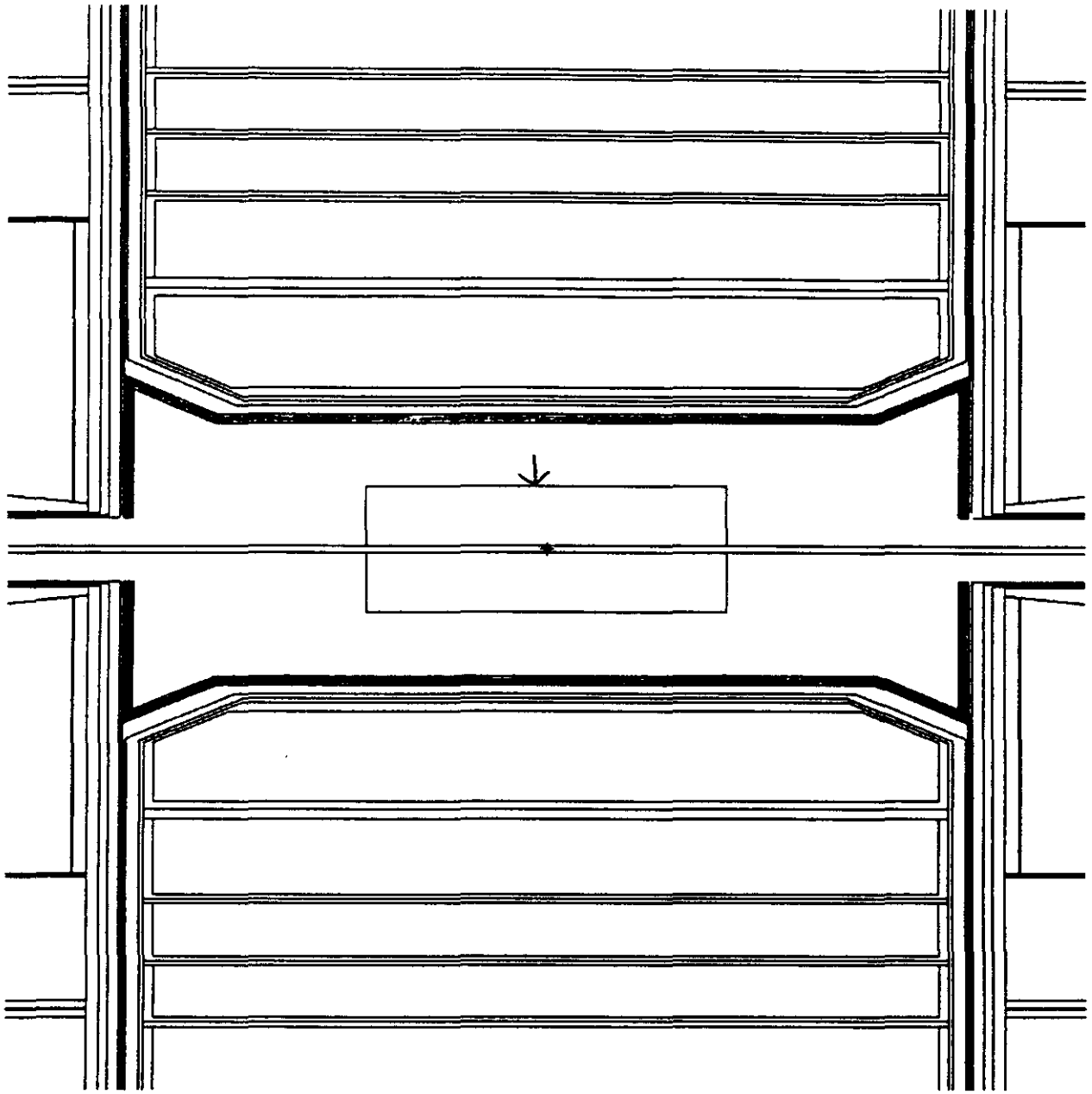

Figure 4: Expanded view of vertex region. B-poly shielding is shaded, and flux is taken across the cylindrical surface marked with an arrow. waters/4-4-92

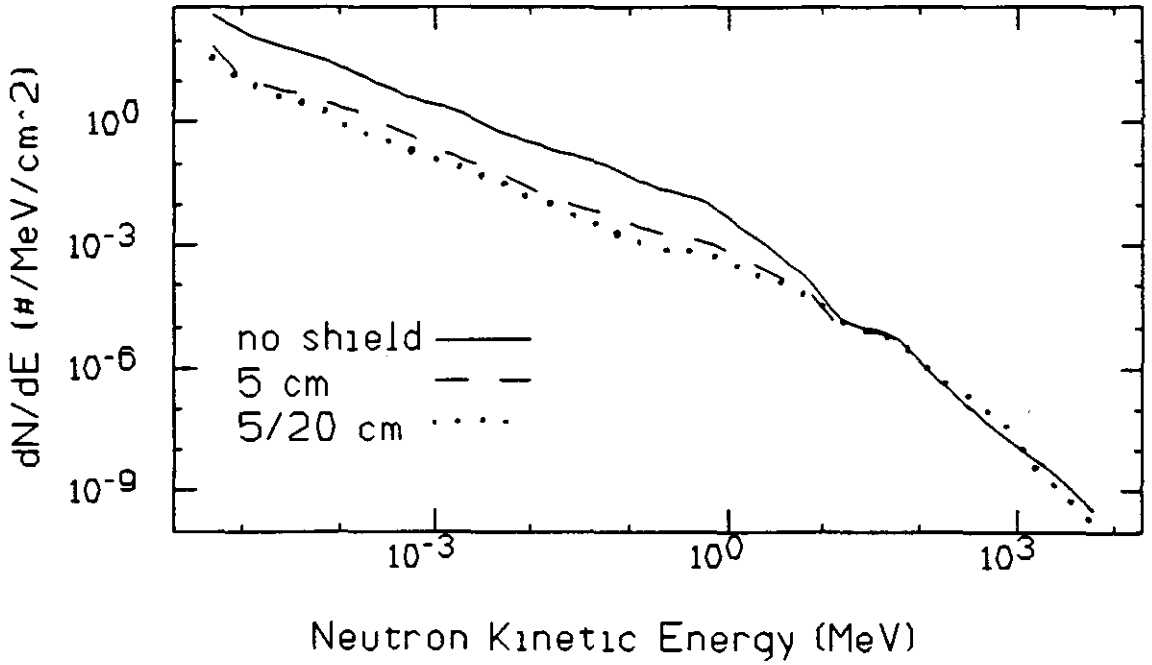

Figure 5: Differential neutron fluence is compared for the no shield, 5 cm and 5/20 cm cases. Results are per SSC minimum bias event. waters/4-4-92

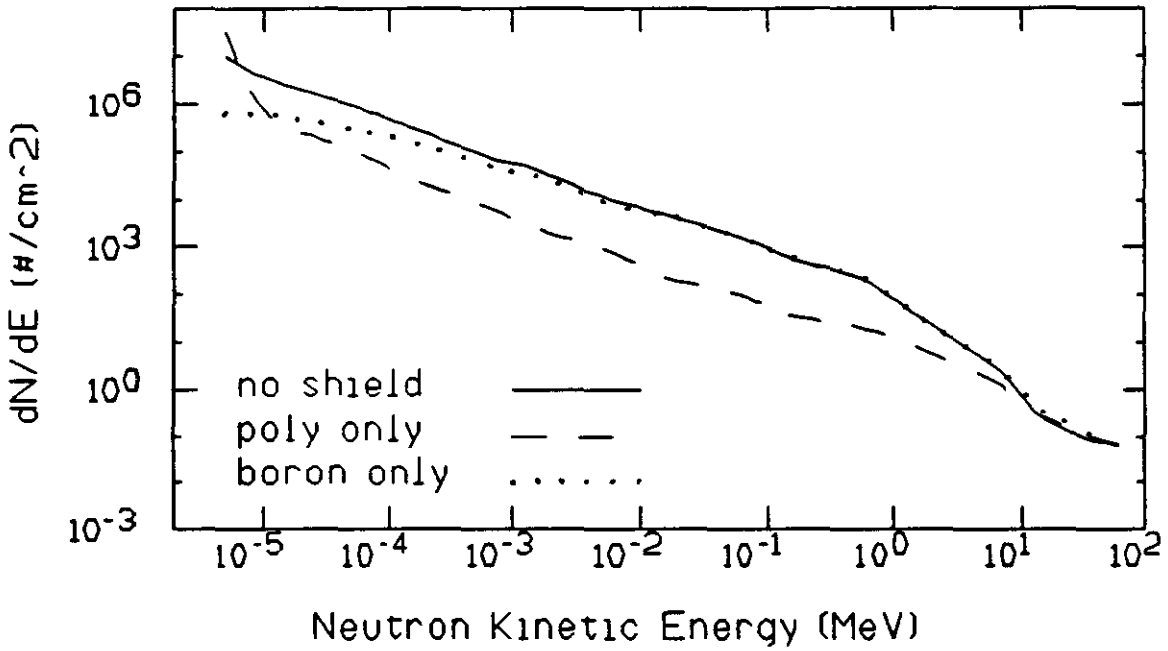

Figure 6: The thermalization effects of shielding composed of just polyethylene, and the supression of the thermal neutrons with a shield composed of just boron are compared to the no shield case. Results are per SSC minimum bias event. waters/4-4-92

cases; this is to be expected since the areas closest to the vertex detector, the EM sections, do not change in composition. Figure 7 shows the differential neutron spectra (dN/dE) similar to figure 5. That same spectra is modified in figure 8 by weighting each bin by the actual particle content (NdN/dE). Figure 9 shows, for the copper case, the fluence components on the 35cm cylindrical surface in increments of 20 cm along the Z axis; little variation is seen over this range. Figure 10 gives a distribution of the neutron flux over the entire surface, again for the 2 energy components. As expected, the lower energy neutrons survive for a long time, crossing the volume many times.

SETUP	Fluence<100 keV	Fluence>100 keV	Total Fluence
no shield	45.30×10^{12}	15.97×10^{12}	61.27×10^{12}
5 cm	5.27×10^{12}	4.03×10^{12}	9.30×10^{12}
5 + 20 cm	3.30×10^{12}	1.90×10^{12}	5.2×10^{12}

Table 3: Fluence through the silicon vertex detector for various thicknesses of borated polyethylene lining. Numbers are in units of 10^{12} per SSC year, per cm^2. waters/4-4-92

SETUP	Fluence<100 keV	Fluence>100 keV	Total Fluence
Uranium HCAL	23.31×10^{12}	13.96×10^{12}	37.27×10^{12}
Copper HCAL	23.68×10^{12}	13.94×10^{12}	37.62×10^{12}
Cu: no FCAL	22.11×10^{12}	13.41×10^{12}	35.62×10^{12}
Cu: no forward	23.56×10^{12}	13.37×10^{12}	36.69×10^{12}

Table 4: Fluence through the silicon vertex detector for four different detector configurations. Numbers are in units of 10^{12} per SSC year, per cm^2. waters/4-4-92

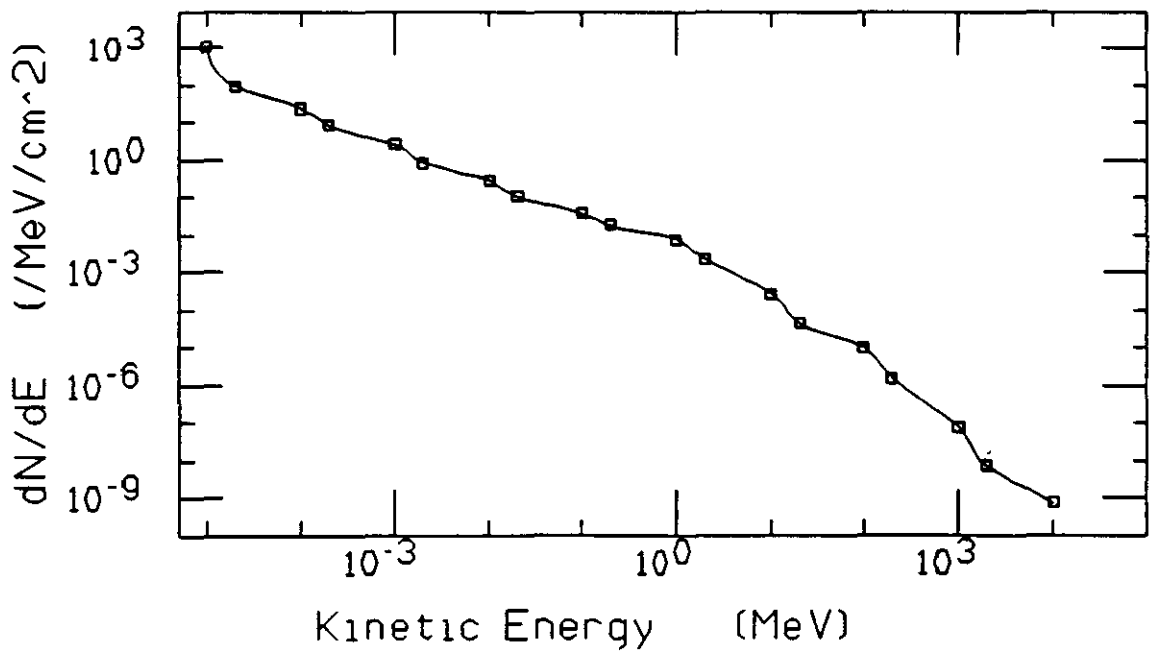

Figure 7: Differential neutron fluence spectrum for the Copper hadronic calorimeter case. Results are per SSC minimum bias event. waters/4-4-92

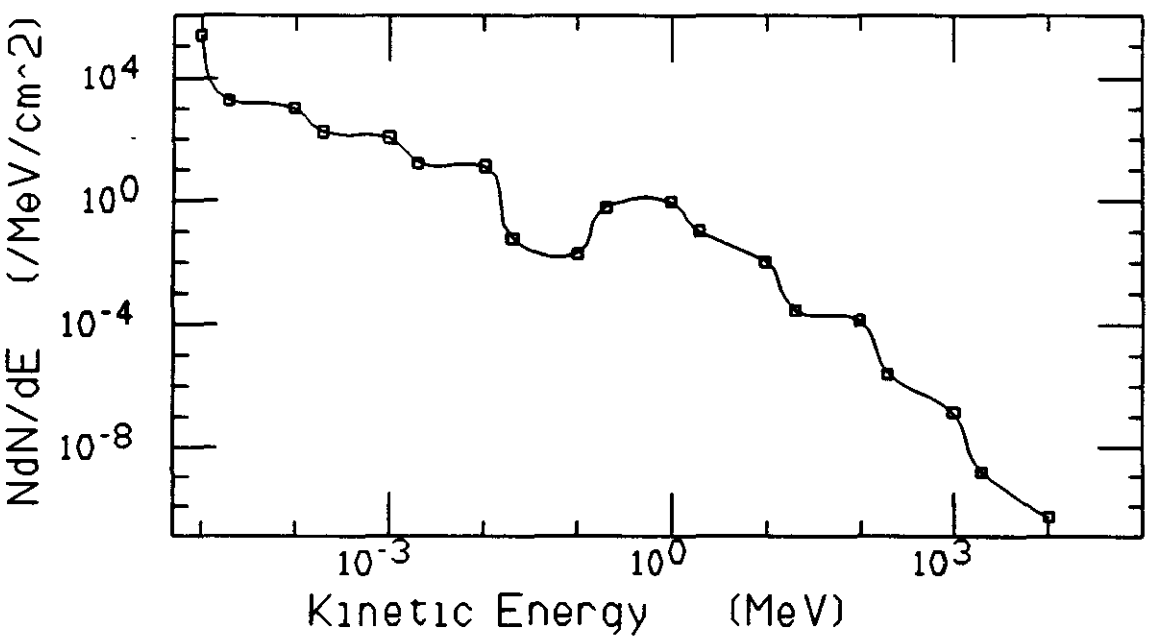

Figure 8: Differential neutron fluence spectrum for the Copper hadronic calorimeter case. Each bin is weighted by the number of particles it actually contains. Results are per SSC minimum bias event. waters/4-4-92

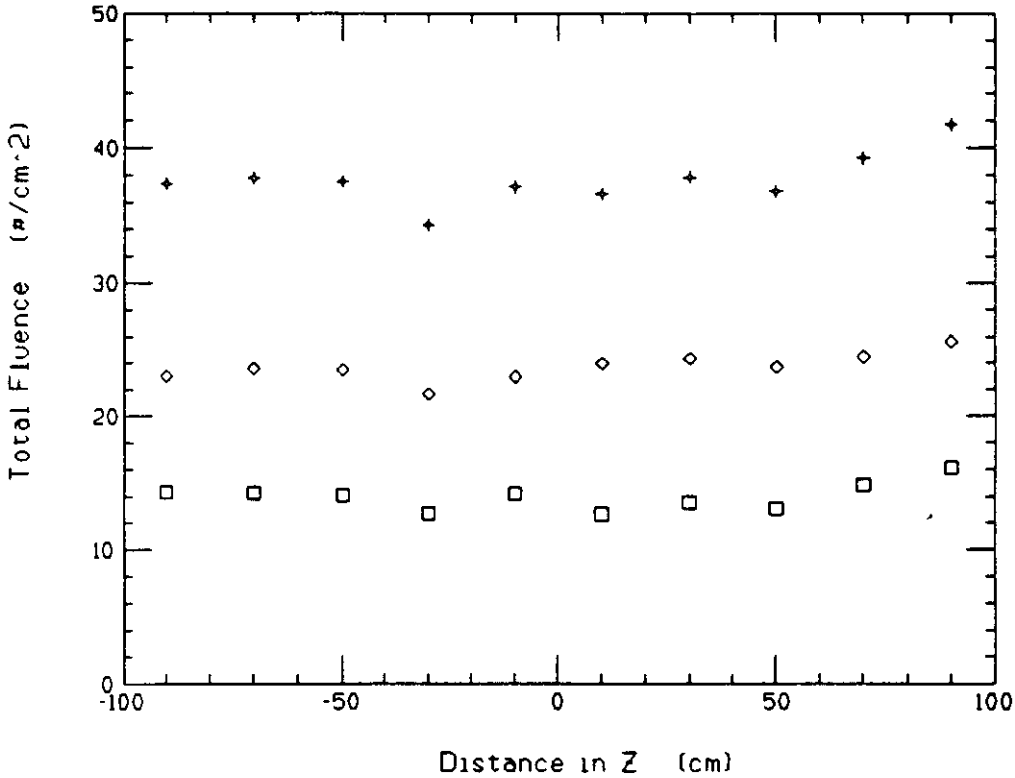

Figure 9: Fluence within 20 cm bins along the silicon vertex cylindrical detector surface. Copper hadronic calorimeter case. Stars: total fluence, Diamonds: particles with energies less than 100 keV, Squares: neutrons with energies greater than 100 keV. Results are in units of 10^{12} neutrons per SSC year per cm^2. waters/4-4-92

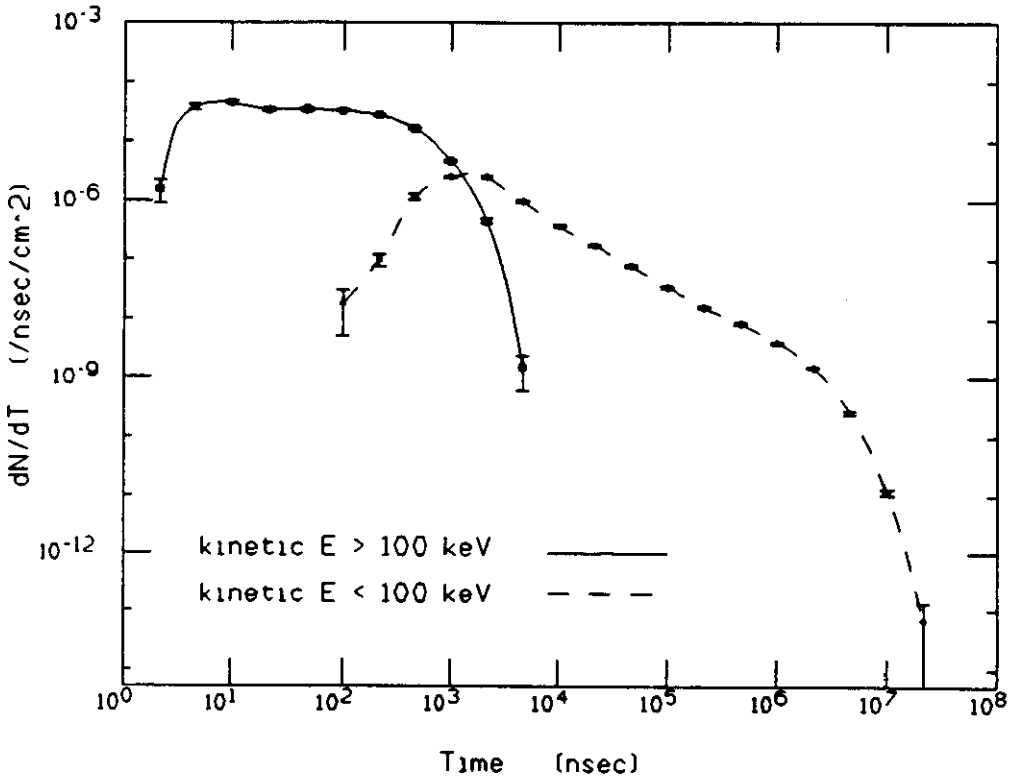

Figure 10: Neutron flux specta for the Copper hadronic calorimeter case. Two different energy components are illustrated. Results are per SSC minimum bias event. waters/4-4-92

6.2.3.2 The Barrel and Endcap Calorimeter

Neutron current data has been obtained at various surfaces of the endcap calorimeter elements. Calculations for the barrel region are now underway. Figure 11 shows a closeup of the endcap region. Table 5 presents the neutron fluence in two energy ranges (total and kinetic energy less than 100 keV) averaged over the five horizontal faces indicated in figure 11. Data from the uranium, copper, copper with no FCAL and copper with no forward elements are presented. Additional data is presented in table 6. Here neutron fluences are calculated along the η=3 excluder line (along with the top of the FCAL from Z=482.6 to 524.96). For both data sets, no difference in fluence is seen at the beginning of the EM section (which was never varied in the four studies). In the Copper studies, the major change comes at the FCAL interface the fluence decreasing as more elements are removed. In the hadronic regions, the uranium study has higher overall fluence, although in both cases the initial showers have played themselves out well before the end of the endcap calorimeter is reached. At this point, what happens in the FCAL and shield/shaper regions dominates the neutron fluence.

Figure 12 presents neutron flux time distributions for the first and last segment of table 6, for the copper case. Figure 13 shows, for the three copper studies, energy distributions for the last segment of table 6. Particle current, not fluence, is illustrated here. Two figures are shown, the first for neutrons with directions 'outward' from the surface (cosine of the angle between surface normal and particle direction from 0.0 to 1.0), and the second for 'inward' directed neutrons (cosine from -1.0 to 0.0).

The barrel and endcap calorimeters meet at Z=2.35 meters. Figure 14 presents total neutron fluence in two energy ranges in 20 cm increments along the line Z=2.35 meters. This region must contain readout and power cables for the vertex detector. One other sensitive area is the the electromagnetic calorimeter in the endcap calorimeter. Figure 15 summarizes the neutron fluence along the vertical planes Z=2.636 meters and Z=309.6 meters, the beginning and end of the EM section in the endcap.

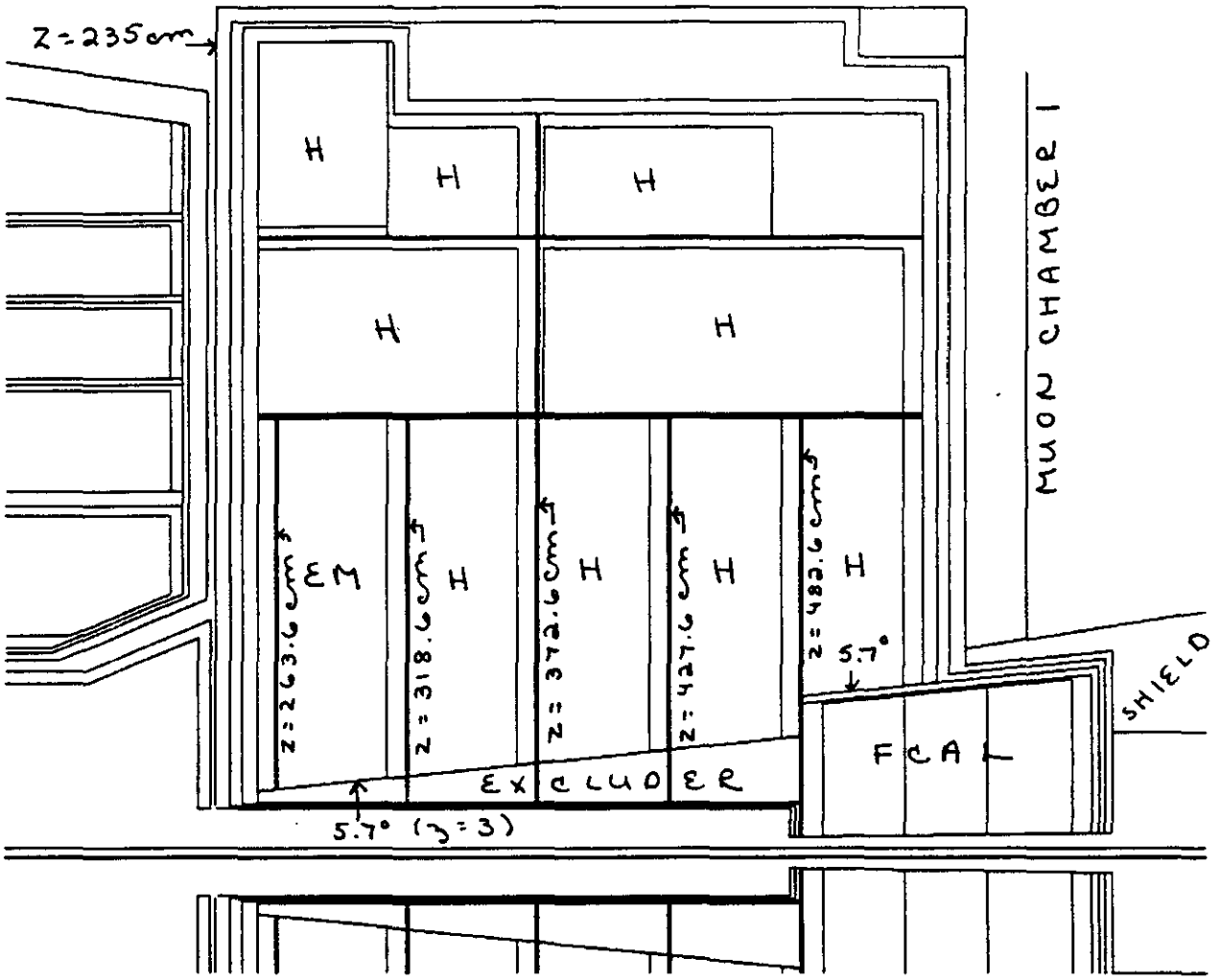

Figure 11: Endcap Calorimeter setup. Spaces between the EM and Hadronic elements are filled with the liquid argon mixture of table 2. The Excluder region is filled with borated polyethylene. Note the position of the Forward Calorimeter (FCAL), and the first Muon Chamber at Z=5.75 meters. A double shell aluminum wall surrounds the Endcap-FCAL-Excluder area. waters/4-4-92

Z distance (cm)	^{238}U	^{64}Cu	^{64}Cu no FCAL	^{64}Cu no fwd
z=263.6	45.1	47.7	43.51	45.83
	26.5	27.1	24.91	26.22
z=318.6	45.3	33.3	30.28	30.39
	25.3	20.2	18.18	18.59
z=372.6	22.7	11.4	10.85	10.79
	12.2	6.2	5.99	5.87
z=427.6	18.1	9.9	8.45	9.24
	9.7	5.3	4.45	4.97
z=482 .6	87.5	85.6	17.11	8.32
	39.4	39.0	9.76	4.15

Table 5: Fluence through the endcap calorimeter at various Z values, between a radius from 5.7 degrees to 180 cm. Numbers are in units of 10^{12} per SSC year, per cm^2. Two lines are given for each interval; the first represents total neutron fluence, the second is the neutron fluence less than 100 keV.

Z range (cm)	^{238}U	^{64}Cu	^{64}Cu no FCAL	^{64}Cu no fwd
z=263.6-309.6	153.2	155.04	142.15	146.93
	60.7	60.09	53.65	55.99
z=318.6-363.6	175.5	76.03	70.85	70.74
	68.9	29.30	27.13	26.09
z=372.6-418.6	113.7	48.09	45.04	48.66
	45.2	17.61	16.78	30.97
z=427.6-473.6	96.5	47.53	37.77	36.74
	38.8	19.11	13.83	12.79
z=482.6-524.96	108.8	100.88	77.91	24.79
	59.4	62.89	42.19	7.73

Table 6: Fluence through the endcap calorimeter along the 5.7 degree angle, within various ranges of Z. Numbers are in units of 10^{12} per SSC year, per cm^2. Two lines are given for each interval; the first represents total neutron fluence, the second is the neutron fluence less than 100 keV.
waters/4-4-92

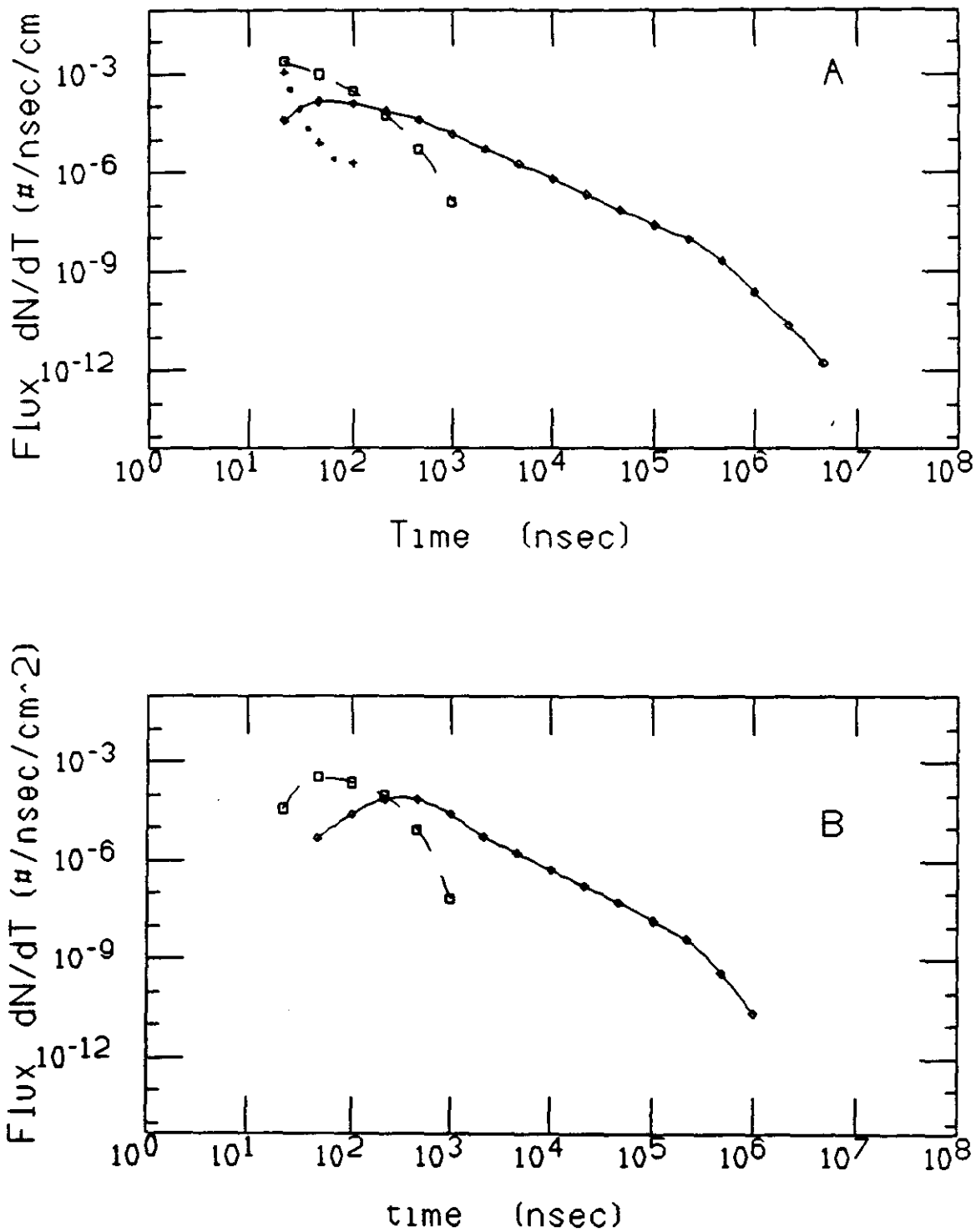

Figure 12: Flux time distributions for the 5.7° segments between 263.6 to 309.6 cm (figure A), and 482.6 to 524.96 cm (figure B). Solid lines represent neutrons with kinetic energies less than 100 keV, dashed lines from 100 keV to 20 MeV, dotted lines greater than 20 MeV. Note the disapearance of the high energy component in B. Note also the overall shifts of the peaks of these distributions in time for the area further from the vertex. Results are per SSC minimum bias event.

waters/4-4-92

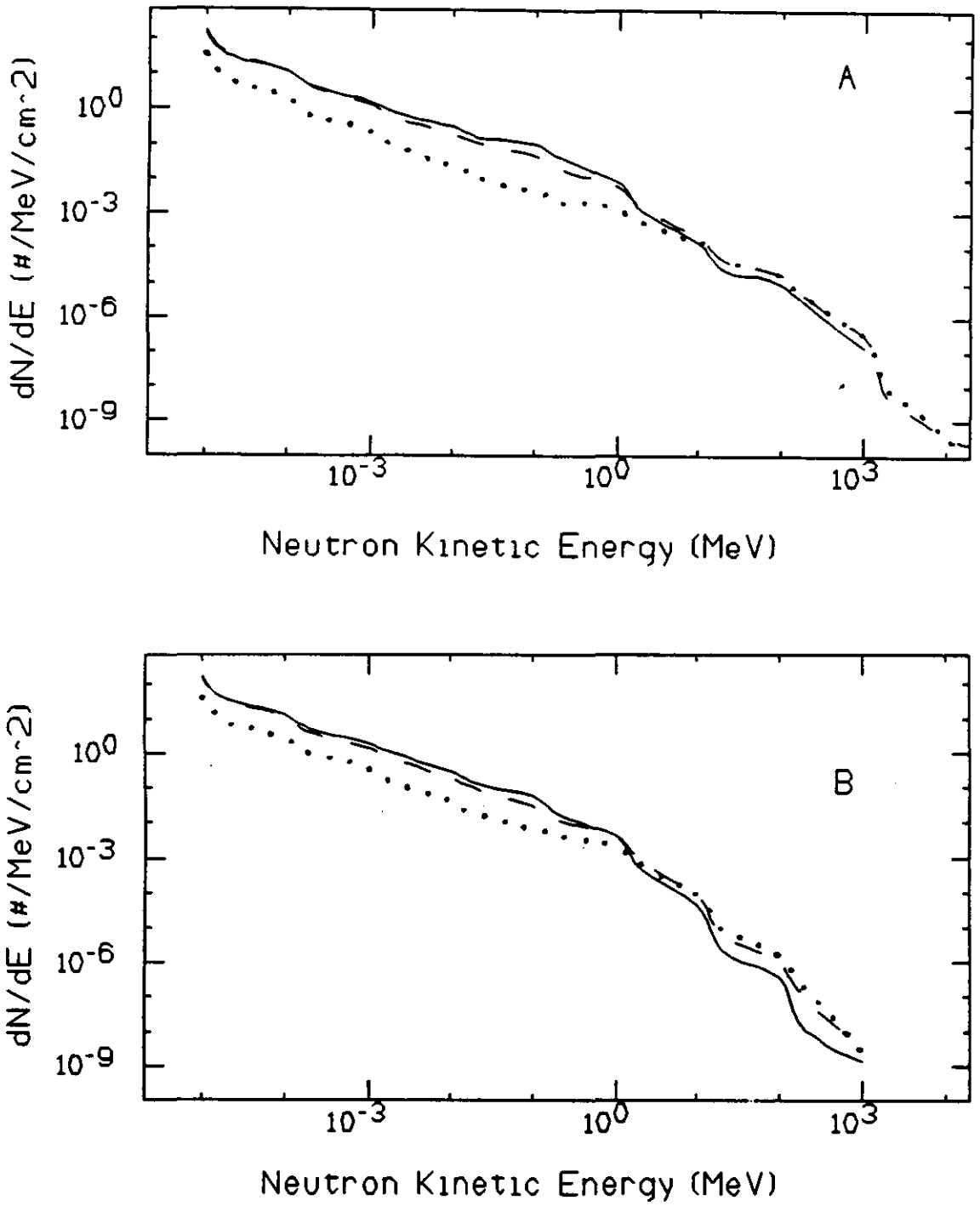

Figure 13: Neutron current (not fluence) energy distributions for the 5.7° segment between 482.6 to 524.96. Solid lines are for the copper case, dashed for copper with no FCAL, and dots for copper with no forward elements. Figure A shows neutrons directed 'outward' from the surface, figure B, directed 'inward'. Results are per SSC minimum bias event.
waters/4-4-92

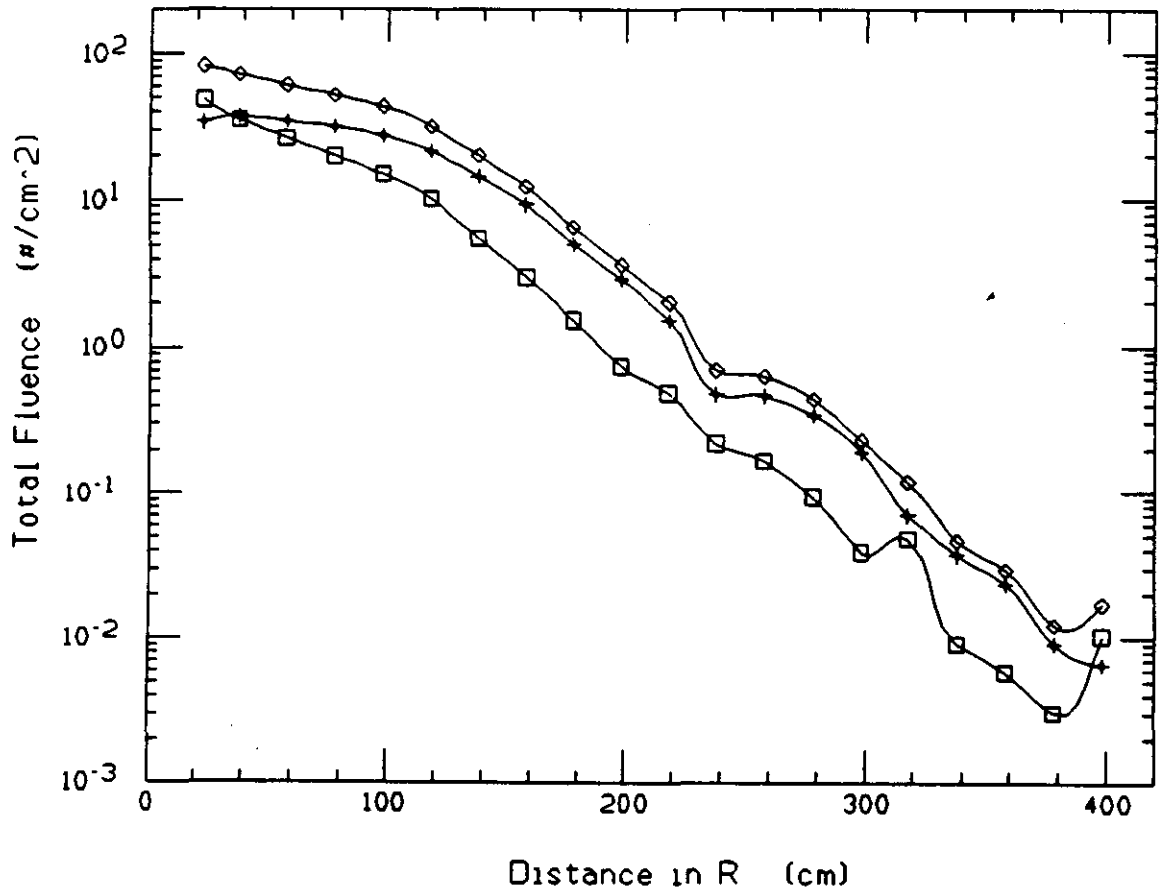

Figure 14: Neutron fluence along 20 cm increments at Z=2.35 meters (division between barrel and endcap calorimeters). Diamonds: total fluence, Stars: fluence for neutrons with kinetic energies less than 100 keVm, Squares: fluence for neutrons with kinetic energies greater than 100 keV. Data are in units of 10^{12} neutrons per cm^2 per SSC year, for the copper calorimeter setup. waters/4-4-92

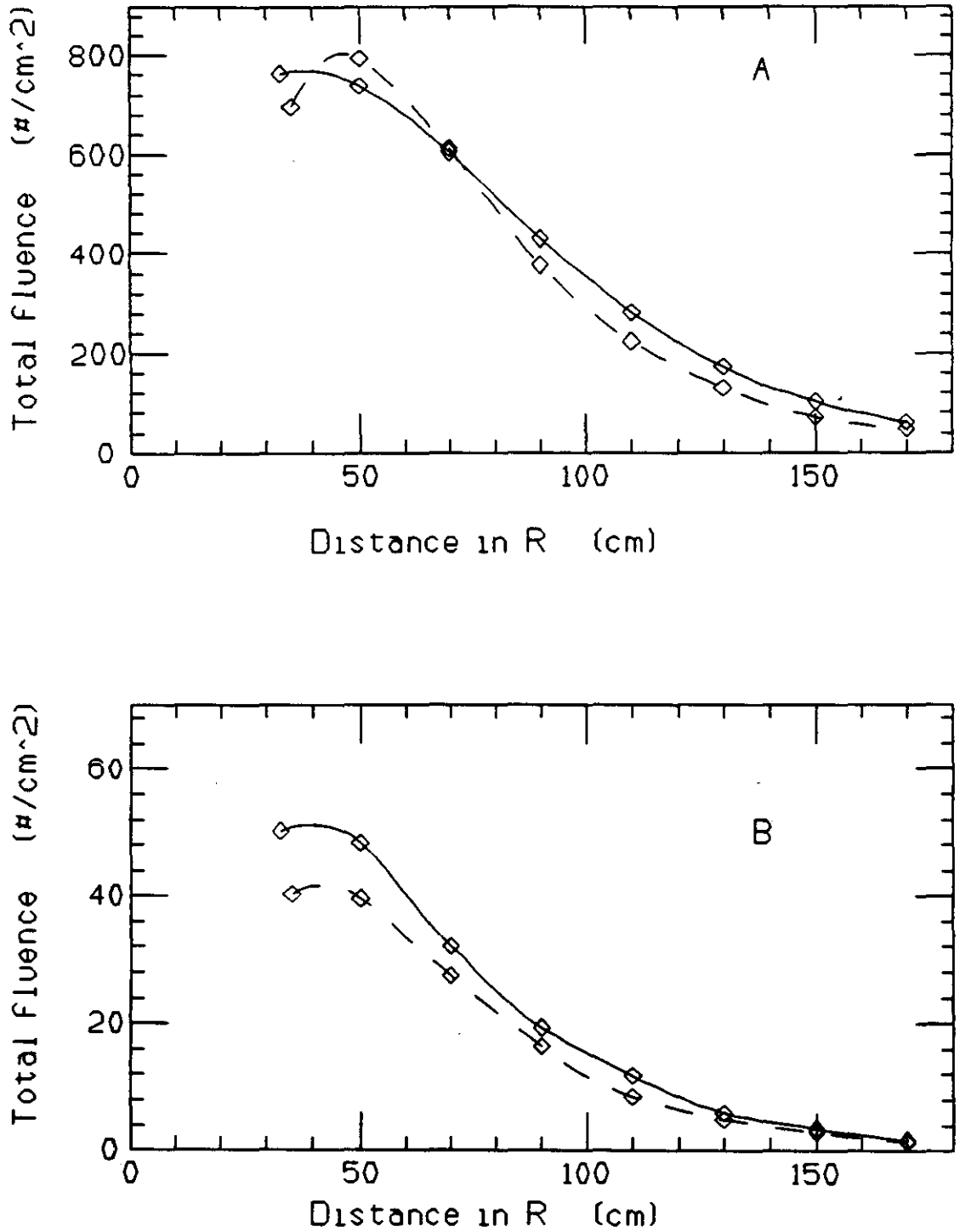

Figure 15: Total neutron fluence along 20 cm radial increments on the planes Z=263.6 cm (solid lines) and Z=309.6 cm (dashed lines) for A) neutrons with kinetic energies less than 100 keV and B) neutrons with kinetic energies greater than 100 keV. Data are in units of 10^{12} neutrons per cm^2 per SSC year, for the copper calorimeter setup. These planes enclose the forward electromagnetic calorimeter section and are important to ascertain possible damage to proposed crystal scintillator material.

waters/4-4-92

6.2.3.3 The Muon Chambers

Neutron fluence data has been calculated for the first muon drift chamber located at Z=5.75 meters. Table 7 summarizes currently available data, and these numbers are plotted in Figure 16. In addition to the usual Uranium, Copper, no FCAL and no Forward Copper studies, the Copper case was modified by including a 5 cm layer of borated polyethylene along the edge of the endcap calorimeter, and the iron shield material just above the FCAL was also replaced with borated poly (see figure 11). Differential energy spectra for the four standard studies are shown in figure 17, for one region close to the beamline, and one far away.

There is little difference in the fluence for the Uranium and Copper cases. The region of the endcap calorimeter closest to the chambers is far enough away from the vertex to no longer be a primary source of neutrons. What happens in the FCAL and more forward regions determines the neutron fluence in this chamber. A slightly higher fluence is seen for the copper case; perhaps a result of longer mean free paths for neutrons in this material.

The FCAL serves as an effective shield for this area. Its removal actually doubles the fluence in the chamber. Figures 18 and 19 attempt to analyze this effect. In figure 18, the neutron currents are plotted for the three copper cases. This data is presented seperately for particles going 'away' (positive Z coordinate of momentum) and 'back toward' (negative P_z) the vertex region. The high energy component with negative P_z for the 'No Forward element' case comes from interactions in the beampipe, which was not removed. Such particles do not have an opportunity to scatter in intervening material, therefore remain high in energy.

The diagrams of figure 19 show, for 1 ISAJET event, the origins of neutrons hitting this chamber. A line representing the first muon chamber is drawn at Z=575 cm, and the upper edge of the FCAL-shield-shaper system is indicated at the bottom of the diagrams. (Note that for the 'No Forward' case, this system is not actually present, but the line has been retained for consistency with the other diagrams.) The endcap calorimeter edge is at 550 cm. For each neutron a line is draw from its radius on the chamber to the radius of its point of origin, either at the edge of the Endcap calorimeter, or on the FCAL-shield-shaper cone. For clarity, only those particles with Y>0.0 for both origin and chamber positions are shown. For each of the three copper cases, neutrons with kinetic energies greater than 100 keV are plotted on top, less than 100 keV on bottom. Note, for the no FCAL case (figures 17C and 17D), the large fluence of higher energy neutrons coming off the shield-shaper element. In addition, of the neutrons crossing the drift chamber plane with P_z <0.0 cam scatter back into the chamber after entering the endcap calorimeter, which is the source of many low energy particles crossing this plane.

These patterns are important to keep in mind when considering the effect of edging the endcap calorimeter with borated polyethylene. As seen in Table 7, substantial reductions are evident in the region closest to the FCAL. Higher up, more neutrons are coming off unshielded forward elements, and have P_z <0.0, and are not influenced by such a lining. These remaining neutrons also tend to have higher energies than the largely thermal spectrum coming directly from the endcap calorimeter.

radii (cm) eta(η)	angles (deg) area (cm^2)	^{238}U	^{64}Cu	^{64}Cu B-Poly	^{64}Cu no FCAL	^{64}Cu no fwd
95.2-115.2	9.4-11.33	6.14	6.54	.81	18.61	5.08
2.5-2.31	13219.8	3.74	4.17	.46	7.79	1.08
115.2-135.2	11.33-13.23	5.18	5.57	1.27	14.65	3.35
2.31-2.15	15733.1	3.17	3.48	.68	6.27	0.69
135.2-155.2	13.23-15.104	3.96	4.83	1.52	11.12	2.48
2.15-2.02	18246.4	2.36	2.90	.89	4.90	0.49
155.2-175.2	15.104-16.95	3.74	4.11	1.51	9.19	1.78
2.02-1.90	20759.6	2.23	2.45	.88	3.89	0.31
175.2-195.2	16.95-18.75	3.24	3.56	1.49	7.52	1.28
1.90-1.80	23272.9	1.95	2.08	.85	3.47	0.27
195.2-215.2	18.75-20.52	2.74	3.31	1.41	6.48	1.05
1.80-1.71	25786.2	1.58	1.86	.86	2.85	0.14
215.2-235.2	20.52-22.25	2.98	2.85	1.33	5.64	0.82
1.71-1.63	28299.5	1.72	1.65	.82	2.68	0.13
235.2-255.2	22.25-23.93	2.14	2.65	1.18	4.96	0.66
1.63-1.55	30812.7	1.23	1.53	.74	2.20	0.08
255.2-275.2	23.93-25.57	2.02	2.31	1.16	4.17	0.59
1.55-1.48	33326.0	1.14	1.32	.72	1.98	0.07
275.2-295.2	25.57-27.17	1.61	2.09	1.16	3.74	0.52
1.48-1.42	35839.3	0.88	1.18	.72	1.71	0.08
295.2-315.2	27.17-28.73	1.46	1.84	1.03	3.06	0.47
1.42-1.36	38352.5	0.83	1.05	.65	1.36	0.04
315.2-323.86	28.73-29.39	1.30	1.67	1.75	2.66	0.36
1.36-1.34	17386.4	0.74	0.92	1.11	1.18	0.04
95.2-315.2	9.4-29.39	2.84	3.27	1.31	6.92	1.29
2.5-1.34	283648.1	1.66	1.93	.79	3.07	0.23

Table 7: Fluence through the muon chamber at Z=575 cm, at various radial intervals. Numbers are in units of 10^{12} per SSC year, per cm^2. Two lines are given for each interval; the first represents total neutron fluence, the second is the neutron fluence less than 100 keV.

waters/4-4-92

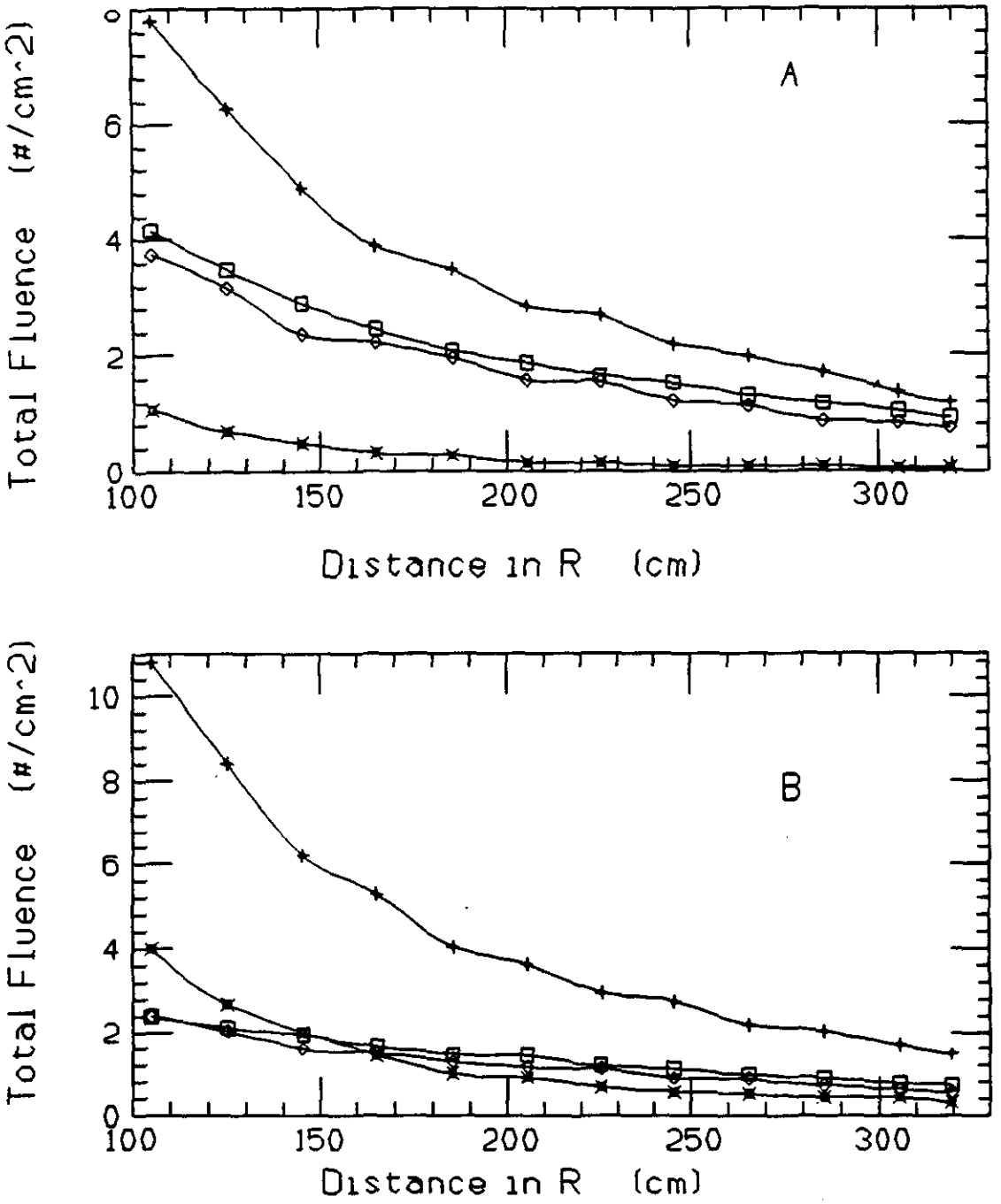

Figure 16: Total neutron fluence within 20 cm increments along the plane at Z=5.75 meters. Data is taken from table 7, and is in units of 10^{12} neutrons per cm^2 per SSC year. A) neutrons with kinetic energies less than 100 keV, B) neutrons with kinetic energies greater than 100 keV. Symbols for both figures are: Diamonds - Uranium setup, Squares - Copper setup, Plus sign - Copper with no FCAL, Cross sign - Copper with no forward elements. waters/4-4-92

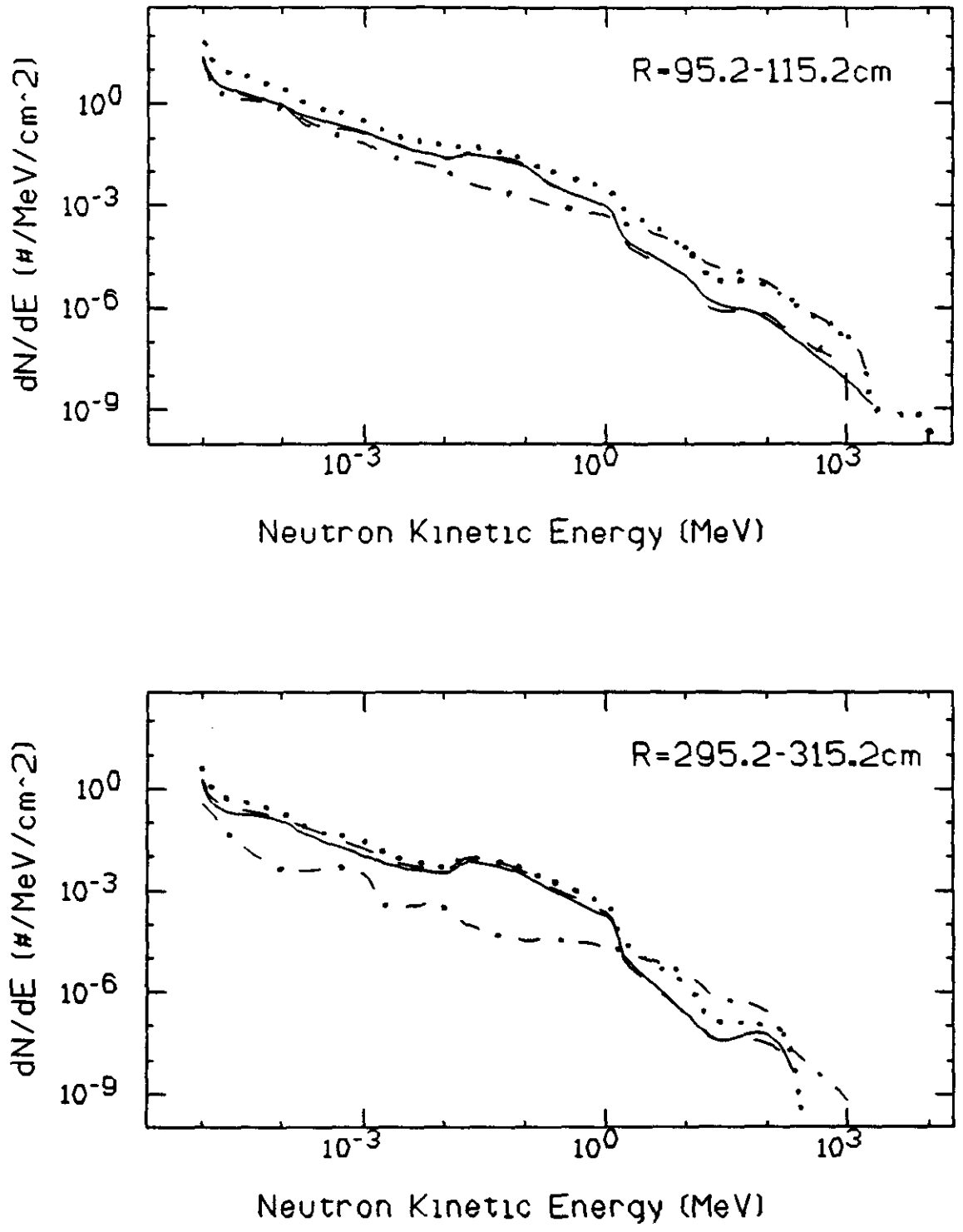

Figure 17: Differential energy distributions for neutron current (not fluence), in two radial segments along the Z=5.75 meter plane. Solid curve is the Uranium case, dashed curve the Copper case, dotted curve, Copper with no FCAL, dot-dash curve, Copper with no forward elements. **waters/4-4-92**

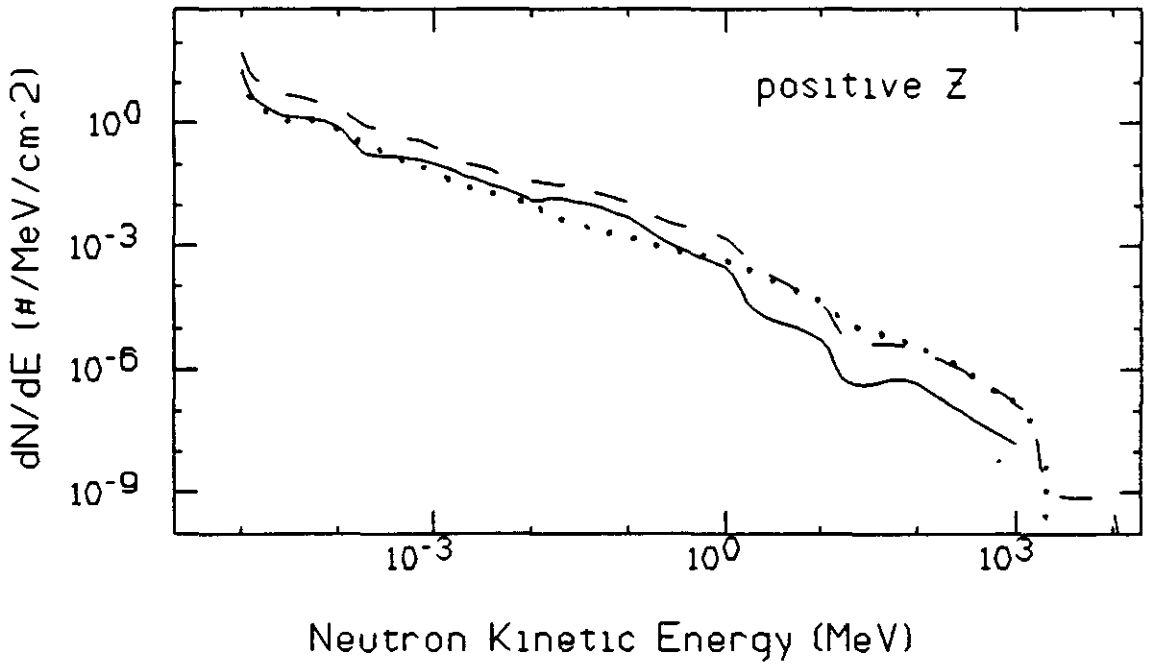

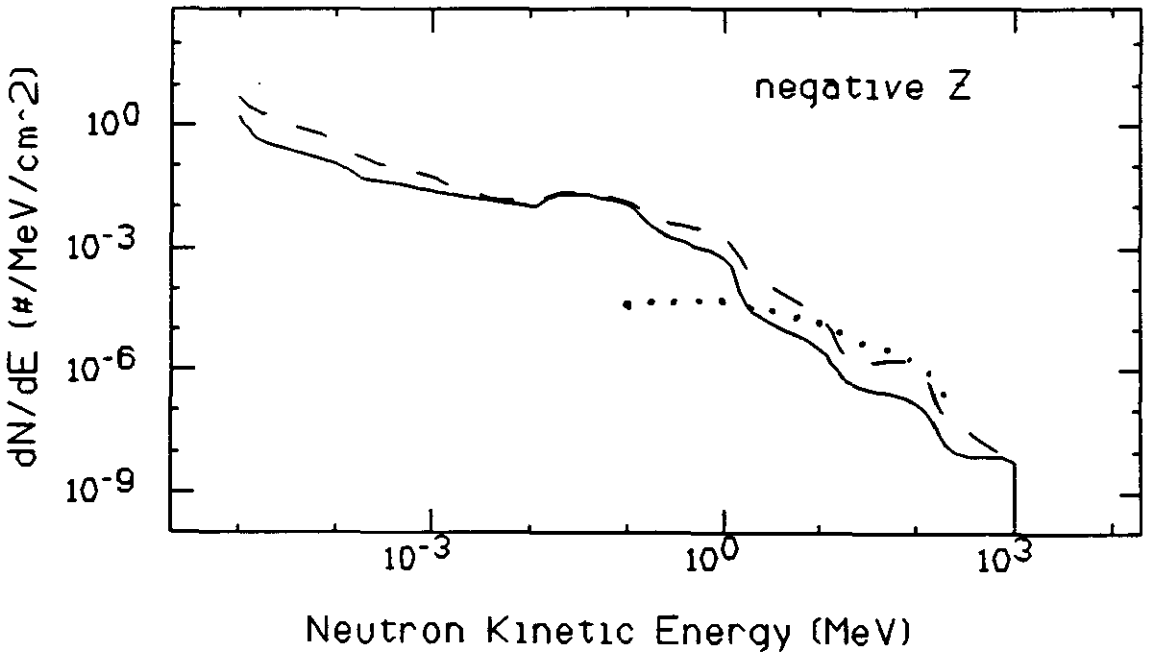

Figure 18: Differential energy distributions for neutron current (not fluence), for the radial segment 95.2-115.2 cm in the Z=5.75 meter plane. Solid curve is the Copper setup, dashed curve, Copper with no FCAL, dotted curve, Copper with no forward elements. The top figure shows all neutrons with Z component of momentum greater than 0.0, the bottom figure has this component less than 0.0. waters/4-4-92

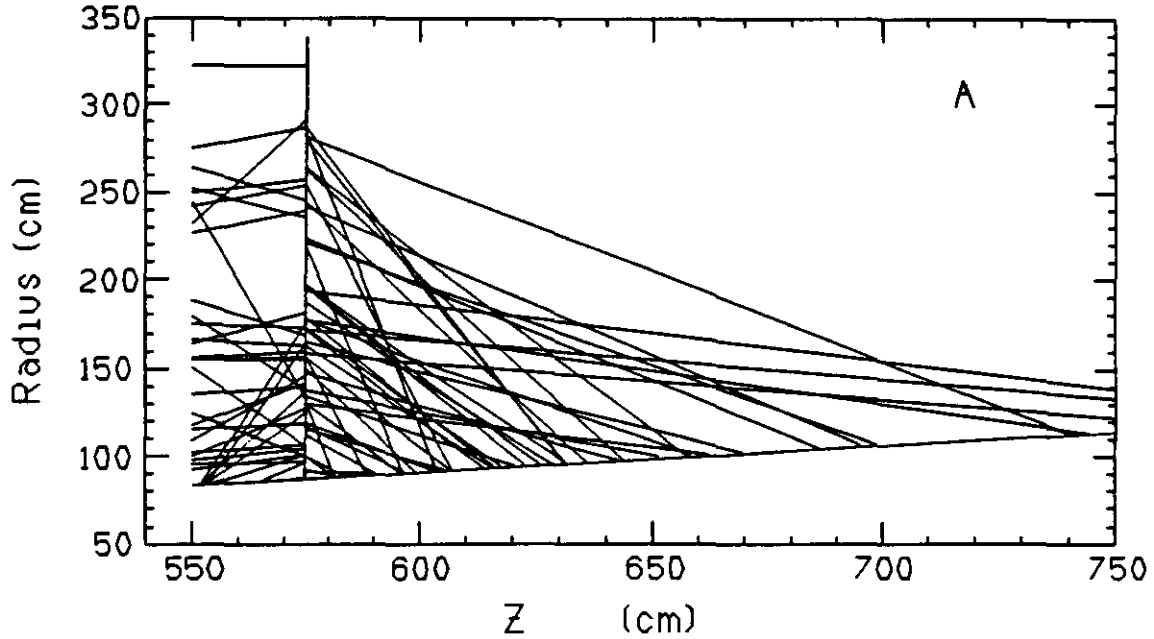

COPPER HADRONIC CALORIMETER

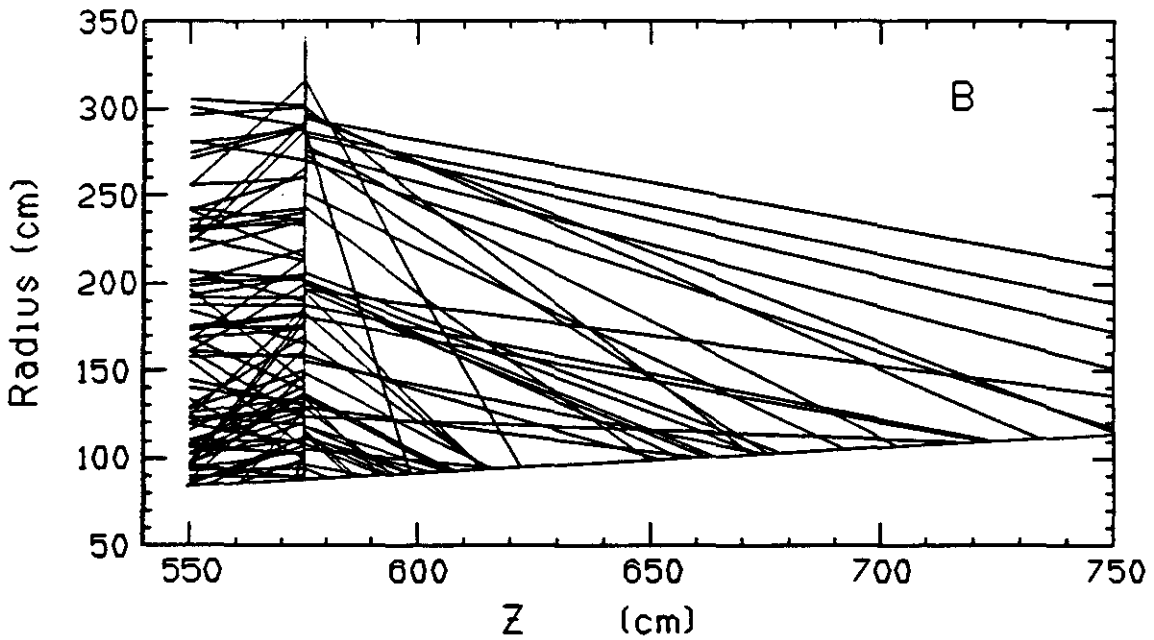

Figure 19: The 6 figures on this and the next two pages show the paths of neutrons hitting the first drift chamber (Z=5.75 m). A and B are for the copper case, C and D for copper with no FCAL, E and F for copper with no forward elements. A, C and E are for neutrons with kinetic energies greater than 100 keV (note, no particle has energy greater than 20 Mev); B, D and F for neutrons with kinetic energies less than 100 keV. Only one SSC event is illustrated. waters/4-4-92

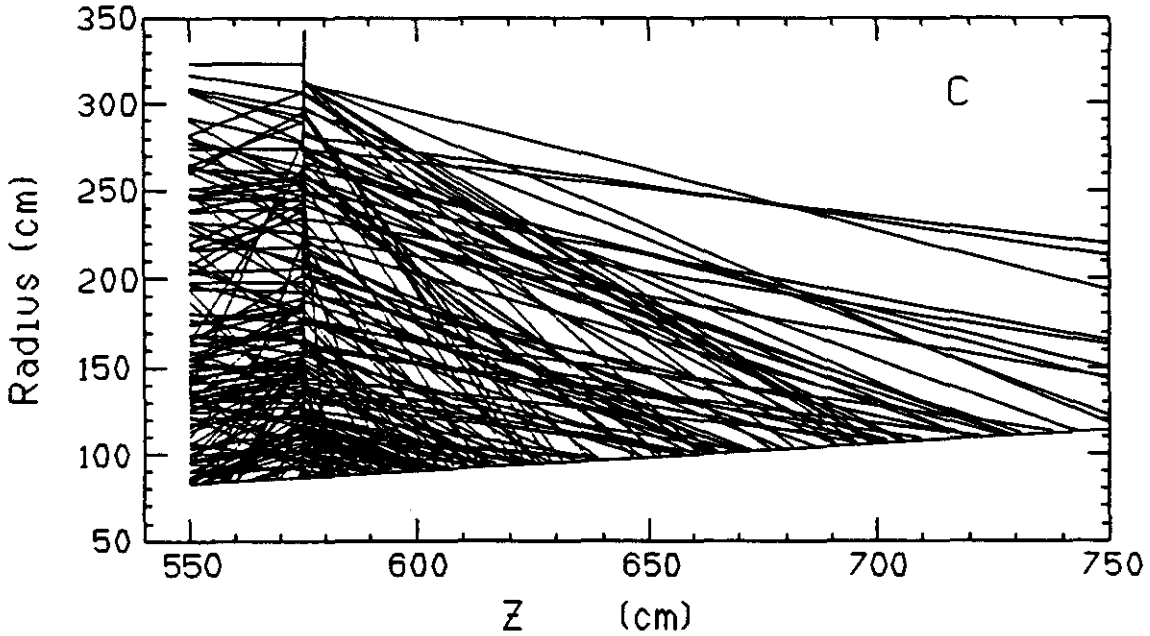

COPPER HADRONIC CALORIMTER: no FCAL

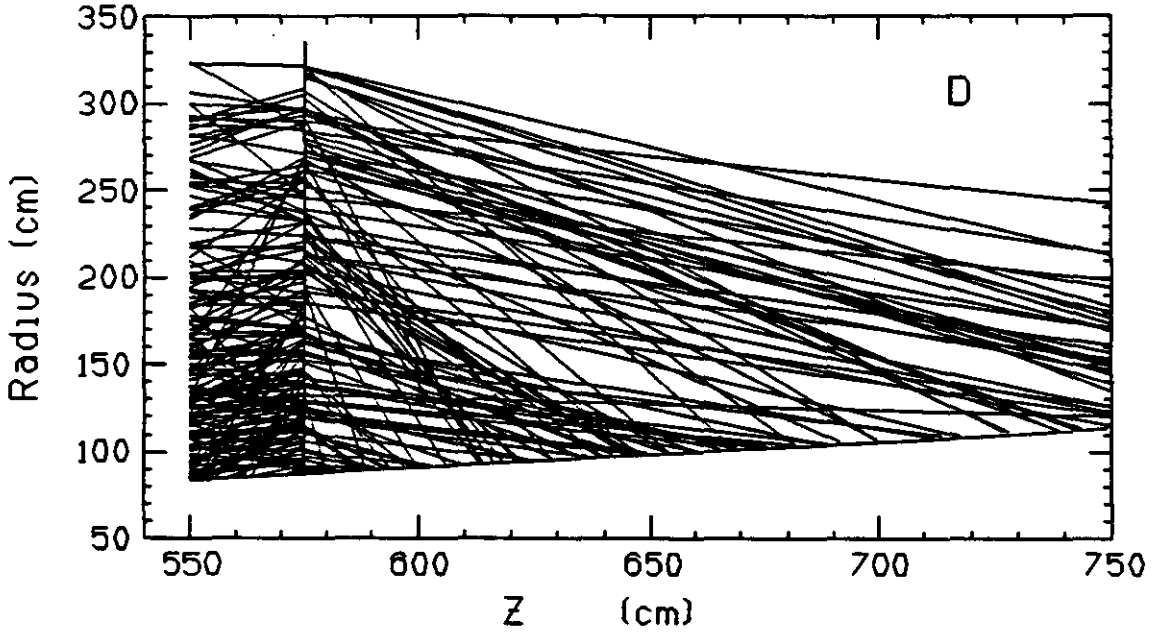

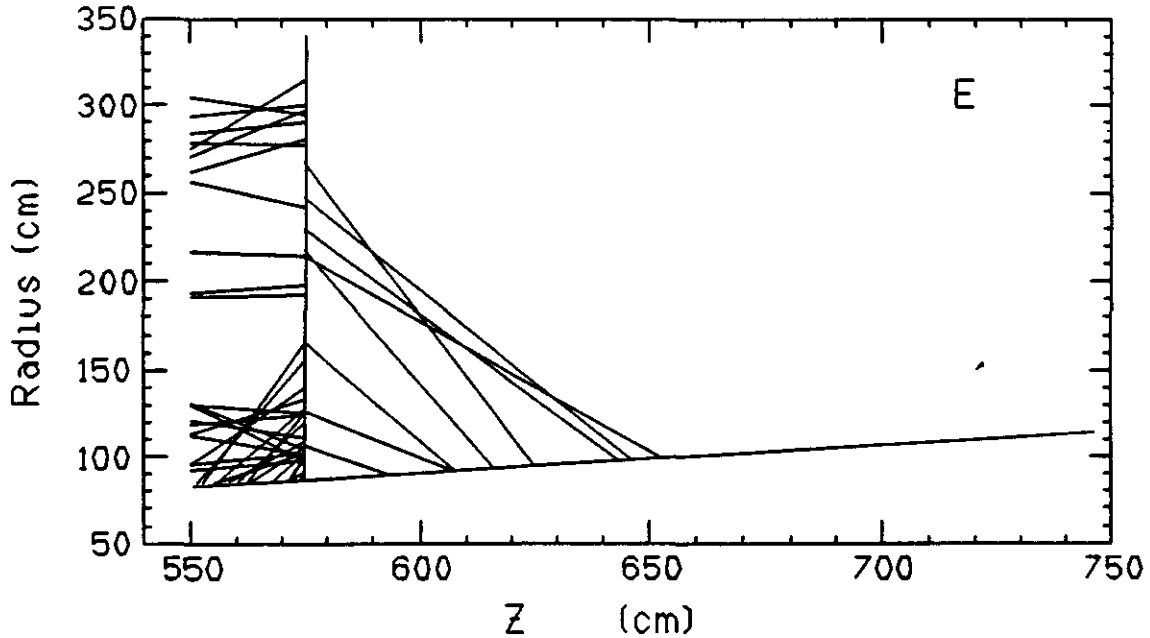

COPPER HADRONIC CALORIMTER: no FORWARD elements

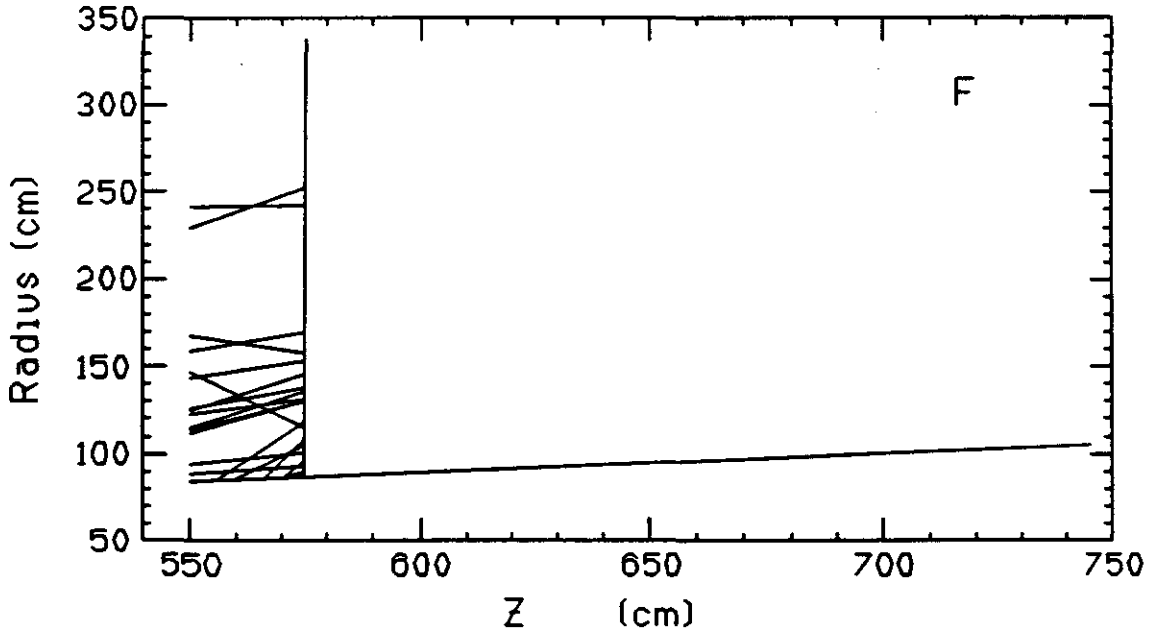

6.2.3.4 The Forward Calorimeter (FCAL)

Table 8 shows the average neutron fluence through various planes perpendicular to the Z axis through the forward calorimeter. There is little difference between the Uranium and Copper cases. This is due to the fact that the FCAL is not located close to the area of the endcap calorimeter where neutrons are produced; primary showers are far out in the longitudinal tails before the FCAL starts. Figure 20 shows, for various neutron energies, profiles of the fluence through the plane Z=525.32 cm in the forward calorimeter for the copper hadronic case. These plots must be interpreted with caution. Results from all 50 ISAJET events are plotted together, and each neutron is weighted by 1.0, rather than the actual particle weight given by the LAHET code. The main purpose of such data is to provide a visual check for possible systematic errors, such as large clumps of particles in one area which may indicate the simulation results are biased by one single shower or jet. Overall, the patterns of all plots seem to be quite uniform in ϕ. Rigorous statistical checks for such problems are available through the LAHET/MCNP package, and will be carried out in the future. (Note, the plots in figure 20 were done by linking standard CERN HBOOK libraries with the LAHET/MCNP package.)

Figure 21 gives two groups of figures which quantify the general trends seen in the plots of figure 20. For each of four planes perpendicular to the Z axis, neutron fluence is given as a function of angle relative to that axis. Data are divided into fluence integrated over all energies, less than 100 keV, 100 keV to 20 MeV, and greater than 20 MeV. Such plots will be used in the calculation of activation of elements. Rather than computing the activation of an entire detector, the calculation may be done for one small segment, and the results scaled for other parts of the detector based on the trend in such fluence profiles[9].

Z distance (cm)	^{238}U	^{64}Cu	^{64}Cu no fcal	^{64}Cu no fwd
z=491.00	585.2	591.23	87.12	32.48
	230.3	232.46	39.84	8.02
z=525.32	1002.6	962.77	90.06	27.19
	431.3	420.58	40.79	5.89
z=559.64	350.6	355.32	96.81	20.43
	157.3	159.82	41.32	3.42
z=593.96	147.3	169.81	111.92	15.75
	66.6	77.70	46.03	1.97

Table 8: Fluence through the forward calorimeter at various Z values. Numbers are in units of 10^{12} per SSC year, per cm^2. Two lines are given for each interval; the first represents total neutron fluence, the second is the neutron fluence less than 100 keV.

waters/4-4-92

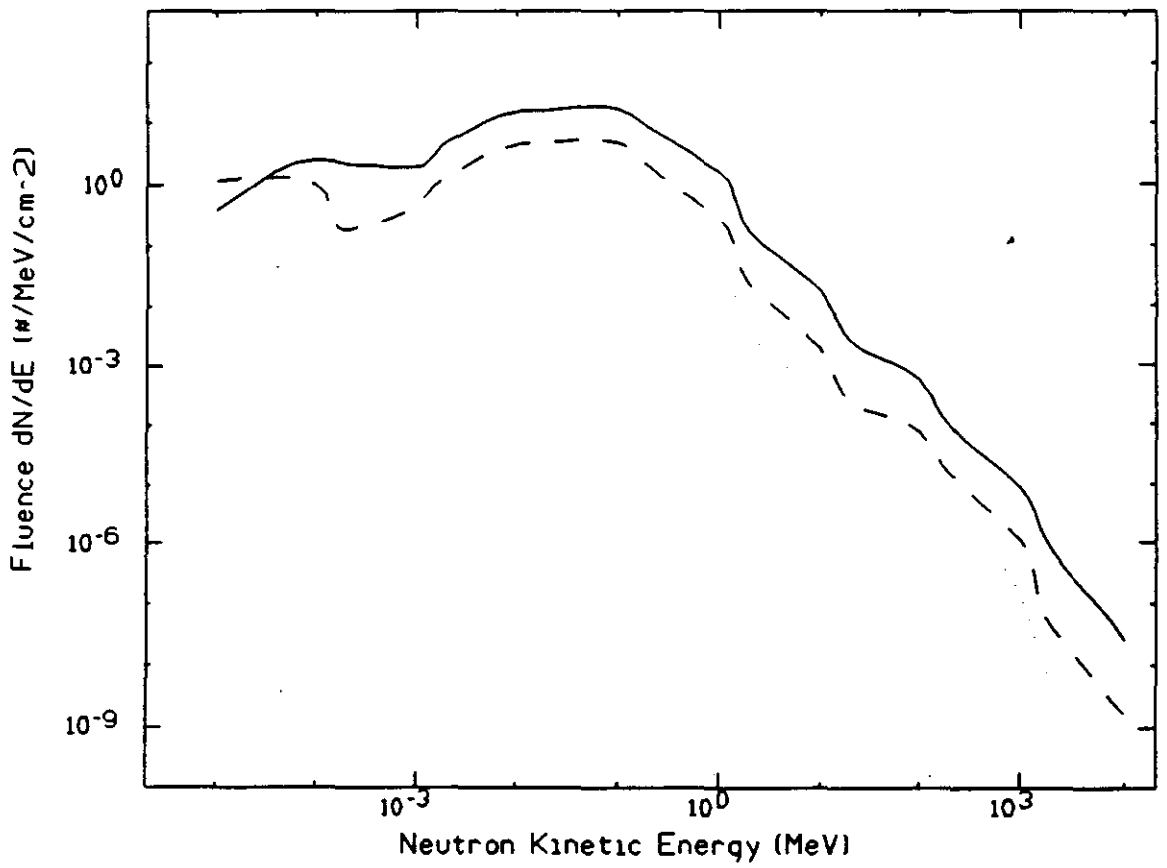

Figure 20: Differential energy distributions for neutron fluence through the plane Z=525.32 cm in the FCAL. Three curves represent different angular ranges: solid = .772° to 2.815°, dashed = 2.815° to 4.857°, dotted = 4.857° to 6.9°. waters/4-12-92

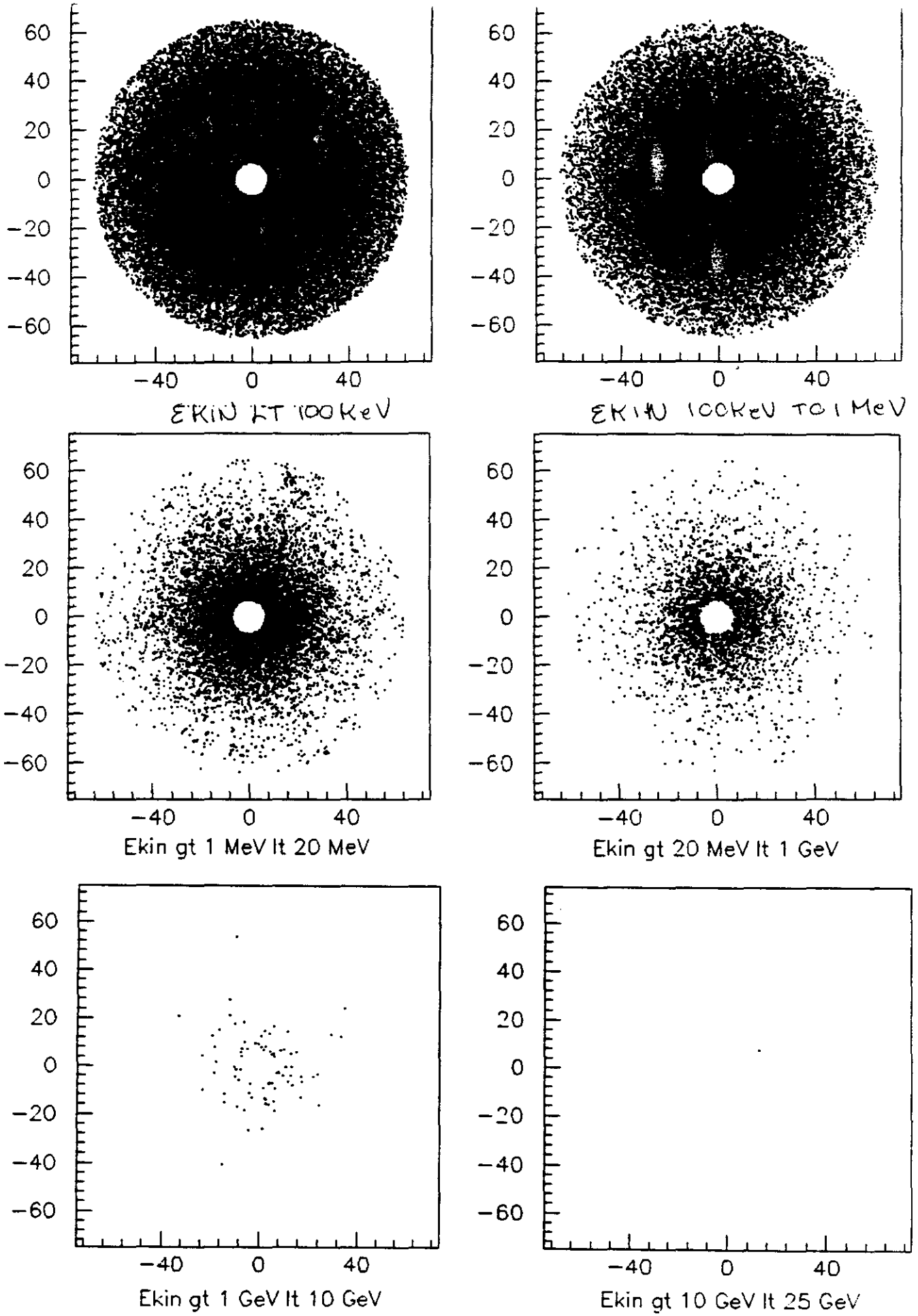

Figure 21: Neutron hit profiles in the Forward Calorimeter at Z=525.32 cm.
waters/4-4-92

Figure 22: This series of 8 figures shows neutron fluence as a function of polar angle θ in four planes perpendicular to the Z axis in the FCAL. Data are divided into total and 3 different energy bins. Units are number per cm^2 per minbias event.
waters/4-4-92

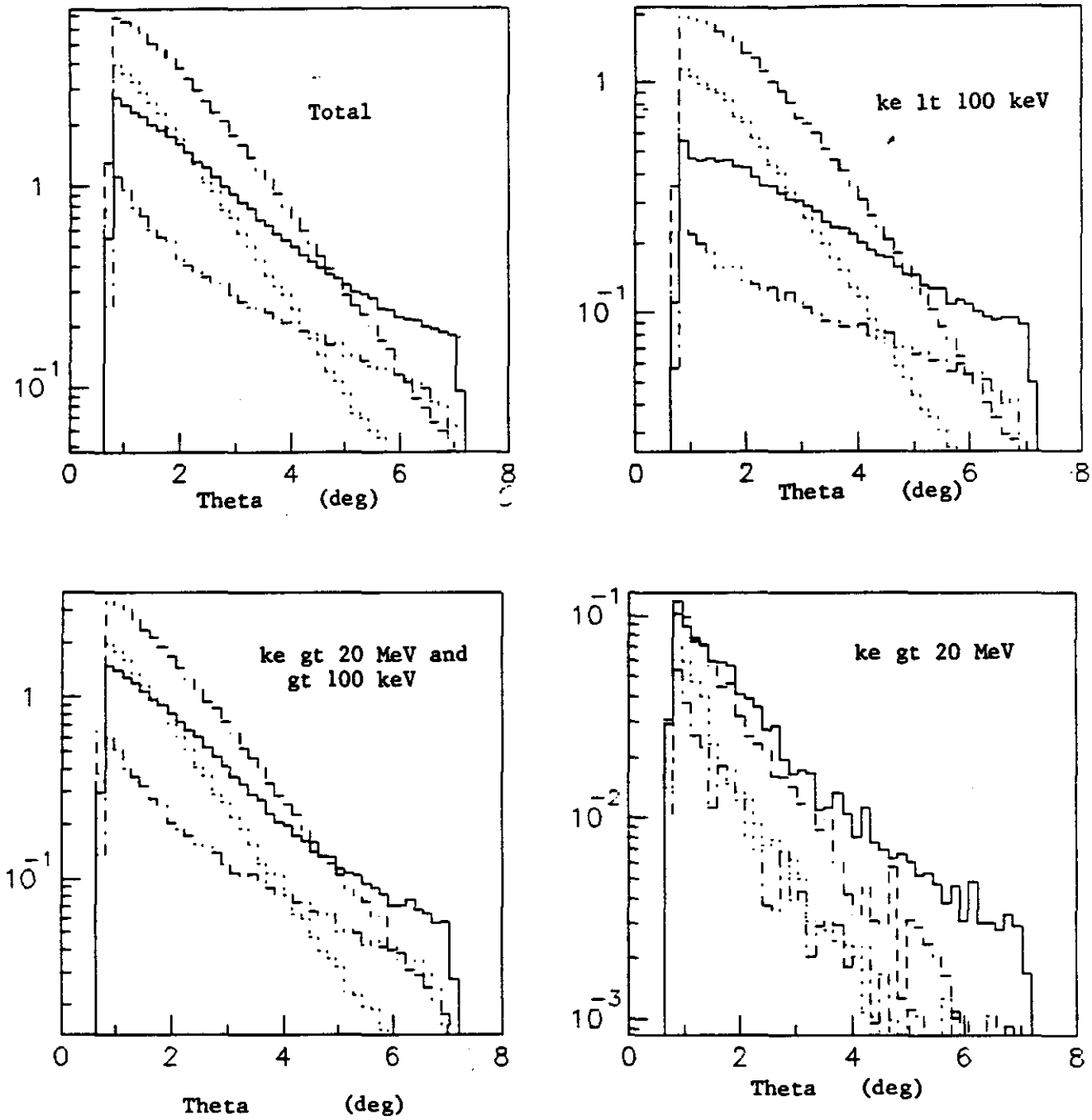

FCAL Neutron Fluence by energy

solid	Z=491.0 cm	dashed	Z=525.32 cm
dots	Z=559.64 cm	dotdash	Z=593.96 cm

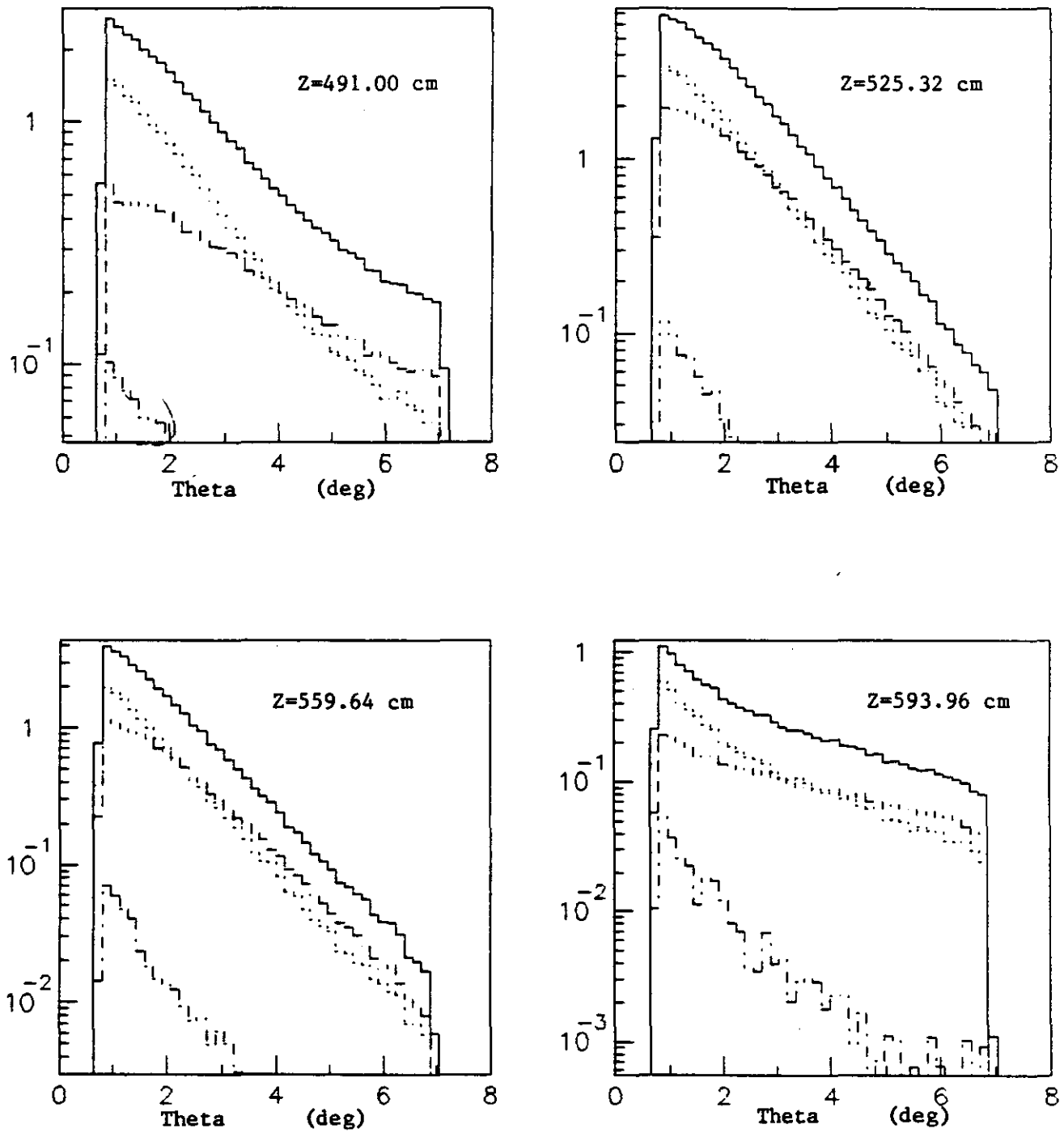

FCAL Neutron Fluence by plane

solid	total
dash	neutron kinetic energy less than 100 keV
dots	neutron ke gt 100 keV, lt 20 MeV
dotdash	neutron ke gt 20 MeV

6.2.3.5 Activation of Elements

The various types of residual nuclei produced in elements of the calorimeter have been tabulated with the LAHET code. These will serve as input into the CINDER90 code, which will follow their decay in order to get an activation profile through time. In determining the dose equivalent to persons working in the vicinity of activated detectors, several factors must be kept in mind. As illustrated in, for example, figure 12, the production of neutrons initiated by primary beam collisions will only last on the order of milliseconds after the beam is turned off, and will not be a source of hazard to persons entering the area. If, however, such effects need to be estimated, table 9 gives fluence to dose conversion factors for neutrons. Heavy charged particles will not make it out of the detector, and electrons will be stopped in the few centimeters of aluminum housing which will be placed around the hadronic calorimeter. The primary worry is low energy photons. CINDER90 will produce an output file of such photons generated within a detector volume. By using this as a source file for MCNP, such radiation may be transported to the site where a person might stand, and appropriate dose equivalents calculated. As of this writing data is being submitted to the CINDER90 code to determine activation in the region of the FCAL and Field Shaper.

Figure 23 presents the LAHET N versus Z distributions, along with the projection on the Z axis for residual nuclei in several areas in GEM. The nuclear line of stability is drawn in for reference. Fissioning nuclei are distinguished by two groups of products distributed slightly below and above one half the Z value of the original nucleus. A typical distribution of fissioning ^{238}U is seen in figure 22B centered around Z=46. A similar, but much reduced indication of the fissioning lead can be detected figure 22F around Z=41. Peaks from reactions with original components Z=18 (Ar), Z~25 (Cr, Mn, Fe, Ni, Cu), and Z~7 (O, N, C), are present in all the plots. This data, along with the low energy neutron flux through the area under consideration, will serve as input into the CINDER90 code.

Avg Neutron Energy (keV)	Factor (10^{-9} Rem/n/cm^2)
7.5	0.992
12	1.08
21	1.73
44	3.06
69	4.35
93	5.47
143	7.61
194	9.61
246	11.5
296	13.3
395	16.5
495	19.7
595	22.6
701	25.3
801	27.3
899	30.2
1012	32.7
2500	40.3
14600	57.9

Table 9: Fluence-to-dose equivalent conversion factors for neutrons. waters/4-4-92

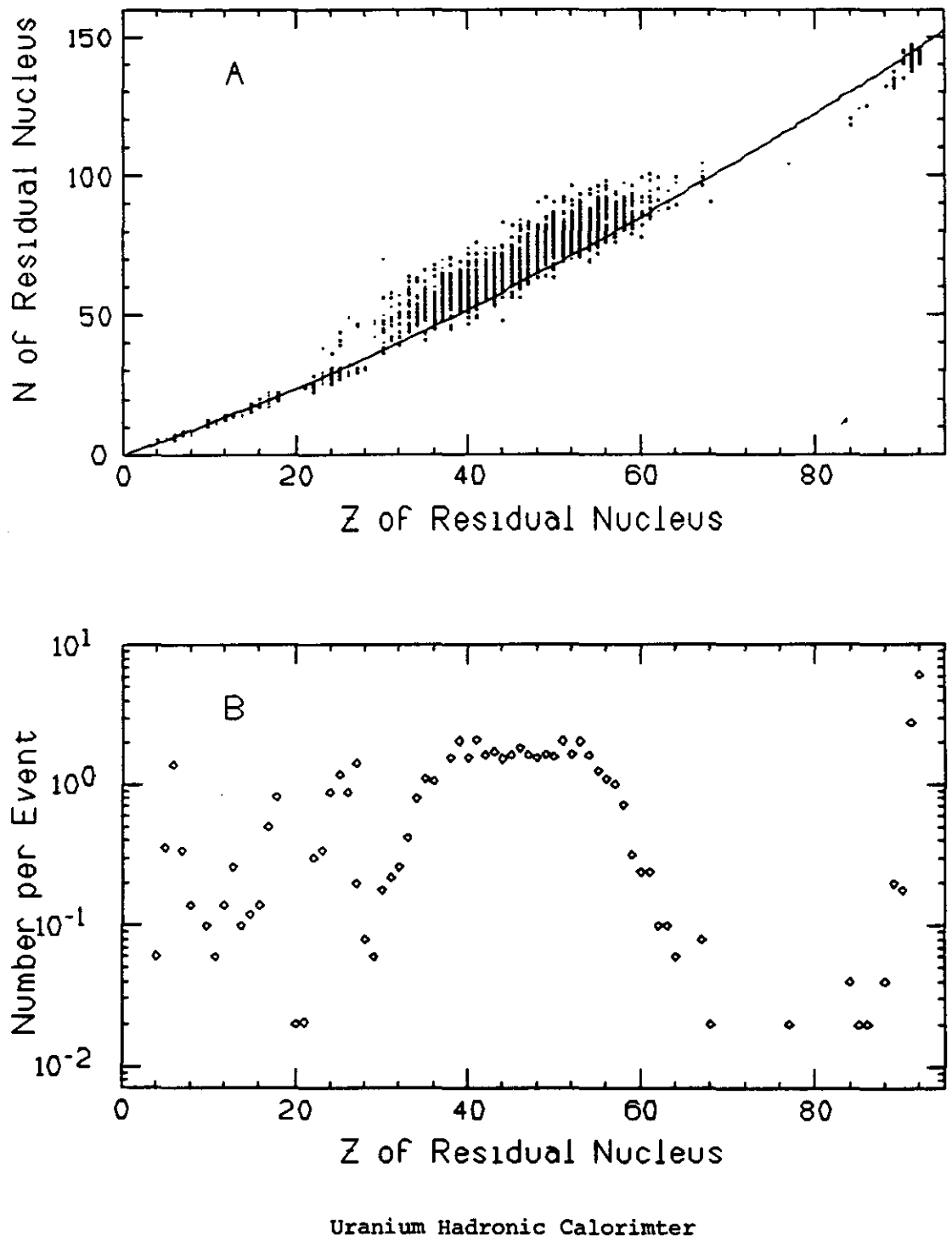

Figure 23: This series of 8 figures shows for A, C, E and G, the N versus Z distribution of residual nuclei, and for B, D, F and H, the projection of these plots on the Z axis. Figures A and B are for the last hadronic calorimeter section closest to the beam pipe for the Uranium setup, and C and D are for the Copper Setup. E and F are for the endcap calorimeter EM section, and G and H are for the FCAL.

waters/4-4-92

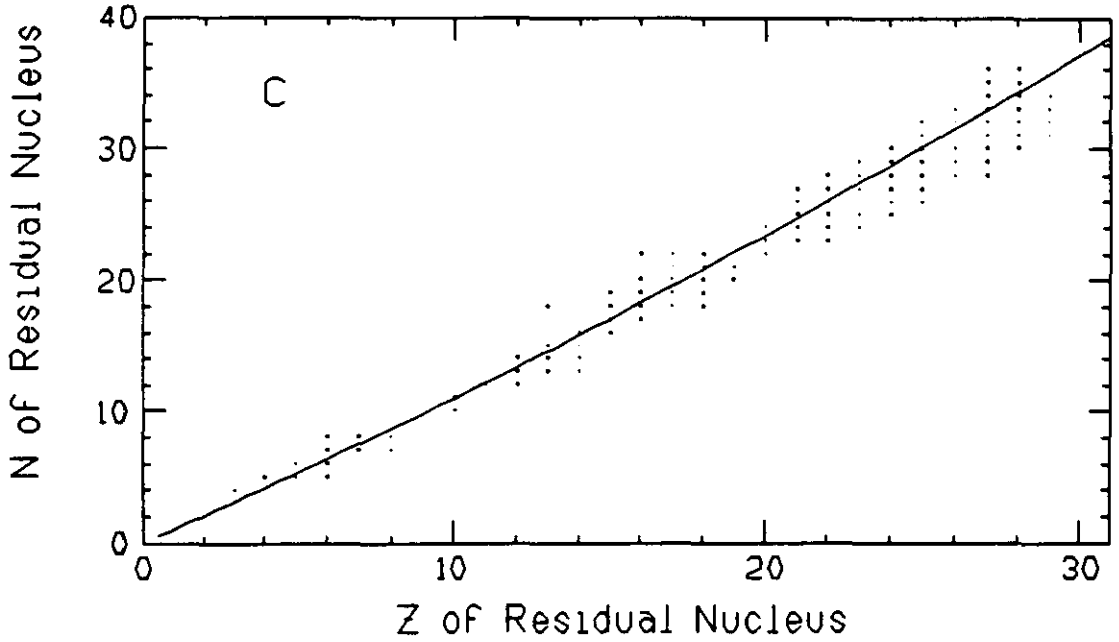

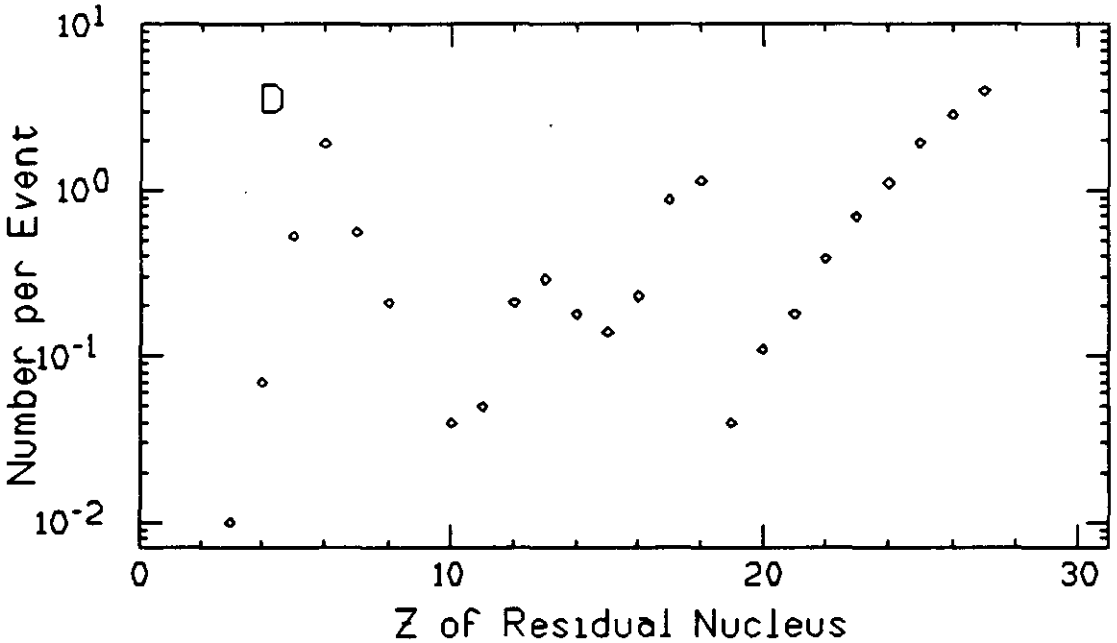

Copper Hadronic Calorimeter

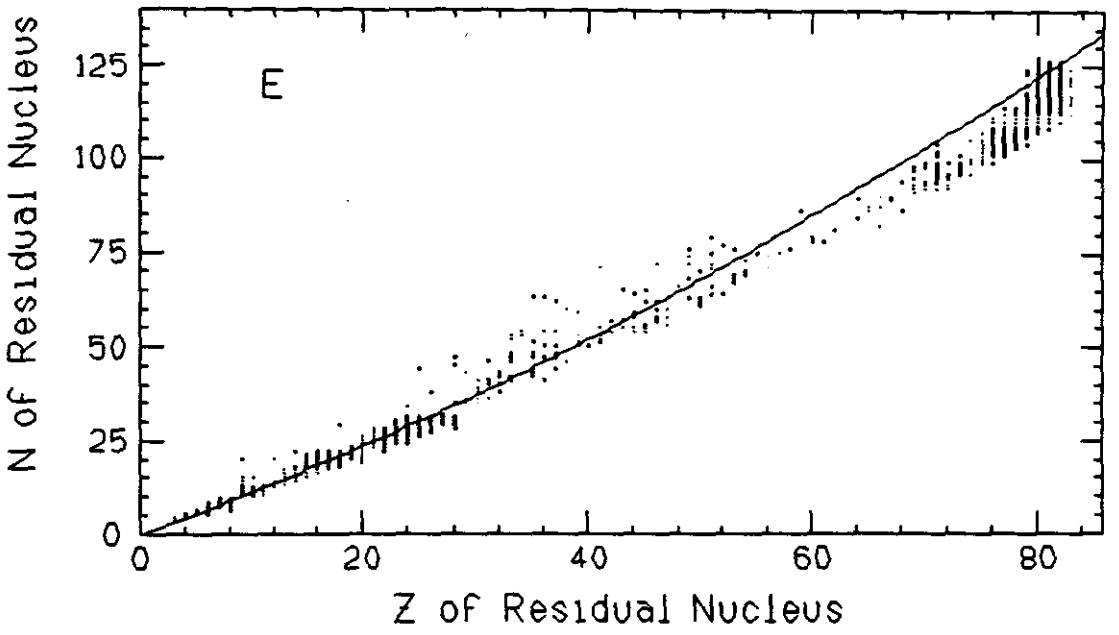

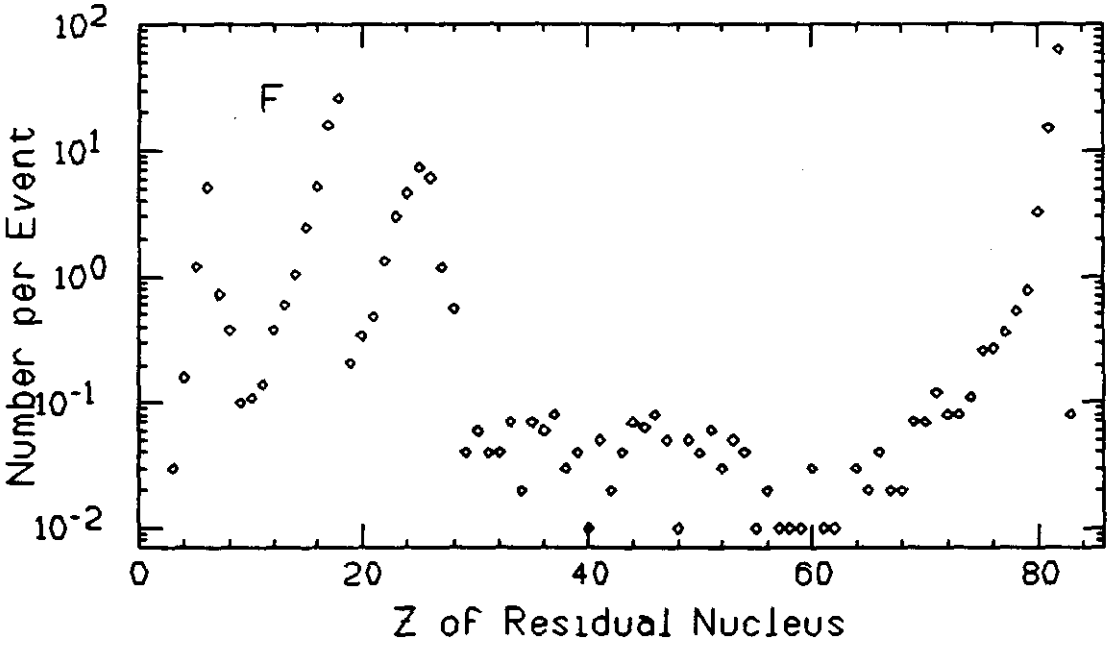

Electromagnetic Calorimeter

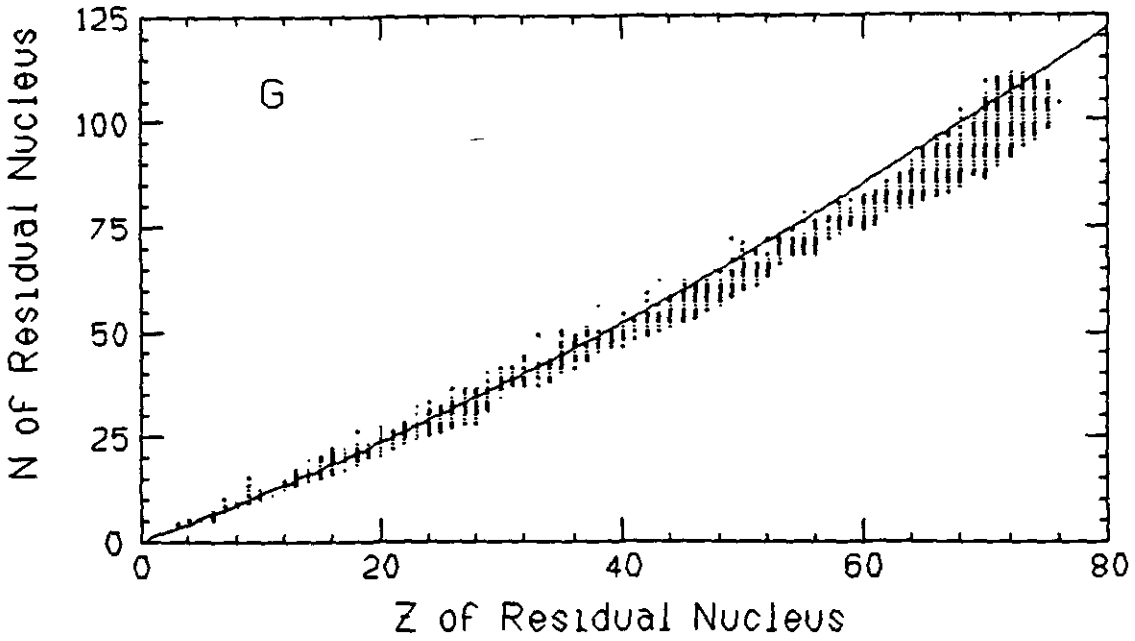

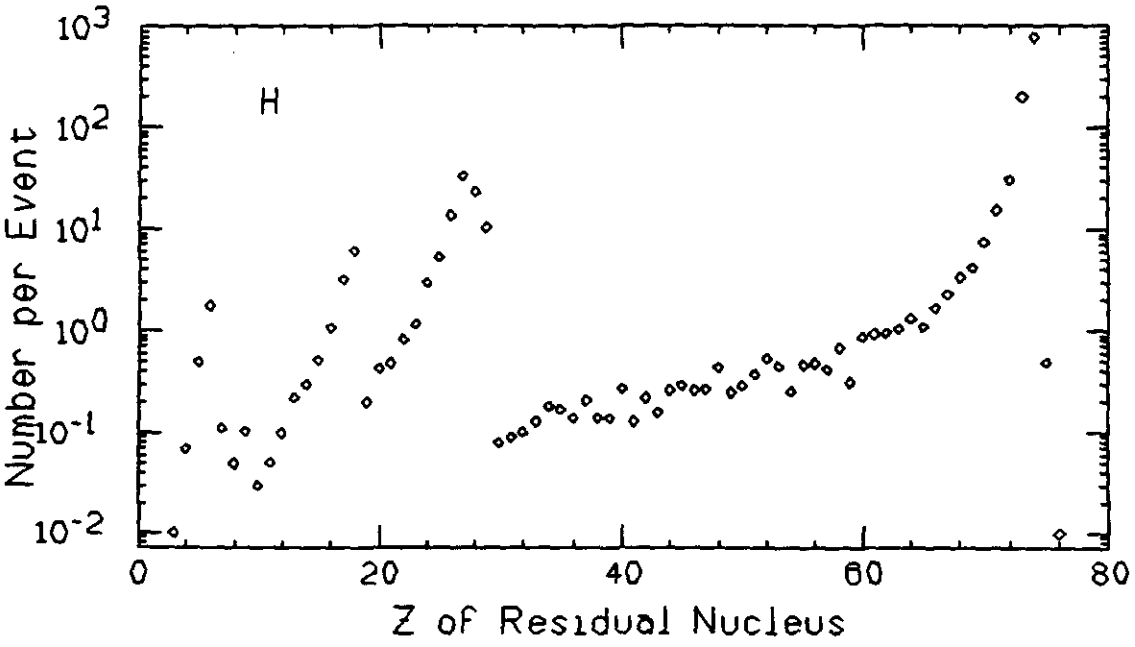

Forward Calorimeter

References

[1] R. E. Prael and H. Lichtenstein, "User Guide to LCS: The LAHET Code System", LAU-UR-89-3014, Los Alamos National Laboratory (Sept 1989)

[2] J. F. Breismeister, ed., "MCNP - A General Monte Carlo Code for Neutron and Photon Transport", LA-7396-M Rev. 2, Los Alamos National Laboratory (1986)

[3] P. A. Aarnio, et. al., "FLUKA89", CERN publication (January 2, 1990)

[4] Radiation Shielding Information Center "HETC Monte-Carlo High-Energy Nucleon-Meson Transport Code", Report CCC-178, Oak Ridge National Laboratory (1977).
R. E. Prael, "Lahet Benchmark Calculations of Differential Neutron Production Cross Sections for 113 MeV and 256 MeV Protons", LA-UR-89-3347, Los Alamos National Laboratory (September 1989).
R. E. Prael, "Lahet Benchmark Calculations of Neutron Yields from Stopping-Length Targets for 113 MeV and 256 MeV Protons", LA-UR-90-1620, Los Alamos National Laboratory (September 1989)

[5] A. Gavron, "Scintillator Efficiency Calculations in a High-Energy Transport-Code Framework", Nuc. Inst. & Meth. A313 (1992) 161-162.
L. Waters, A. Gavron, "Applications of the Lahet Simulation Code to Relativistic Heavy Ion Detectors", Proceedings of the Symposium on RHIC Detector R&D, October 10-11, 1991, BNL 52321, Brookhaven National Laboratory

[6] W. R. Nelson, H. Hirayma and D. W. O. Rogers, "The EGS4 Code System", SLAC-265 (December 1985)

[7] T. R. England, "CINDER-A One-Point Depletion and Fission Product Program", Bettis Atomic Power Laboratory report WAPD-TM-334 (August 1962; revised June 1964).
R. R. England, R. Wilczynski and N. L. Whittemore, "CINDER-7: An Interim Users Report," Los Alamos Scientific Laboratory report LA-5885-MS (April 1975).
W. B. Wilson, et. al., "Status of CINDER and ENDF/b-V Based Libraries for Transmutation Calculations", Proc. Int. Conf. and Nuclear Waste Transmutation, July 22-24, 1980, Austin, Texas (March 1981) p. 673.
W. B. Wilson, et. al., "CINDER-3: Depletion Code for Class VI Computers", Trans. Am. Nucl. Soc. 46, 724 (1984)

[8] D. E. Groom, ed., "Preliminary Version: Radiation in the SSC Interaction Regions", Task Force Report, SSC-SR-1033 (Feb 18, 1988).
D. E. Groom for the Task Force on Radiation Levels in the SSC Interaction Regions, SSC-229 (July 21, 1989)

[9] W. B. Wilson, T. R. England, W. W. Kinnison and D. M. Lee, "Calculation of the Production and Decay of Radionuclides in the Hadron Calorimeter of the L* Detector of the SSC", LA-UR-91-999, Los Alamos National Laboratory (March 4, 1991).
D. M. Lee, W. W. Kinnison and W. B. Wilson, "A Prediction of the Neutron and Charted Particle Backgrounds in the L* Detector", presented at the Symposium on Detector Research and Development for the SSC, Oct 15-18, 1990, Fort Worth, Texas; LANL preprint LA-UR 90-3449.
D. M. Lee, W. W. Kinnison and W. B. Wilson, "A Monte Carlo Calculation of the Neutron Flux in the L* Detector", presented to the IEEE Nuclear Science Symposium, December 1990, LANL preprint LA-UR 90-2954

[10] F. E. Paige and Serban D. Protopopescu, "ISAJET 6.34, A Monte Carlo Event Generator for P-P and Pbar-P Reactions", Brookhaven National Laboratory